1   **Trace element composition of scheelite**

2   Marjorie Sciuba[1,2], Georges Beaudoin[1,2], Donald Grzela[1,2], Sheida Makvandi[1,2,3]

3   ✉ Marjorie Sciuba

4   Marjorie.Sciuba.1@ulaval.ca

5   ✉ Georges Beaudoin

6   Georges.Beaudoin@ggl.ulaval.ca

7   1 Département de Géologie et Génie Géologique, Université Laval, Québec (QC) G1V 0A6, Canada

8   2 Centre de recherche sur la géologie et l'ingénierie des ressources minérales (E4m)

9   3 COREM, 1180 Rue de la Minéralogie, Québec, Canada, G1N 1X7

10

11

12   **Abstract** Scheelite from twenty-five representative orogenic gold deposits from various geological settings was

13   investigated by EPMA (Electron Probe Micro-Analyzer) and LA-ICP-MS (Laser Ablation-Inductively Coupled Plasma-Mass

14   Spectrometer) to establish discriminant geochemical features to constrain indicator mineral surveys for gold exploration.

15   Scheelite from orogenic gold deposits displays five REE patterns including a bell-shaped pattern with a (i) positive or (ii)

16   negative Eu anomaly; iii) a flat pattern with a positive Eu anomaly and, less commonly, iv) a LREE enriched pattern, and v)

17   a HREE enriched pattern. The REE patterns are interpreted to reflect the source of the auriferous hydrothermal fluids and,

18   perhaps, co-precipitating mineral phases. Scheelite from deposits formed in rocks metamorphosed at upper greenschist to

19   lower amphibolite facies have low contents in REE, Y, and Sr, and high contents in Mn, Nb, Ta and V, compared to scheelite

20   formed in rocks metamorphosed below the middle greenschist facies. Scheelite from deposits hosted in sedimentary rocks has

21   high Sr, Pb, U and Th, and low Na, REE and Y, compared to that hosted in felsic to intermediate rocks. Statistical analysis

22   including elemental plots and multivariate statistics with PLS-DA (Partial Least Square-Discriminant Analysis) reveal that

23   the metamorphic facies of the host rocks, as well, as the regional host rock composition exert a strong control on scheelite

24   composition. This is a result of fluid-rock exchange during fluid flow to gold deposition site. PLS-DA and elemental ratio

25   plots show that scheelite from orogenic gold deposits have distinct Sr, Mo, Eu, As and Sr/Mo, but indistinguishable REE

26   signatures, compared to scheelite from other deposit types.

27   **Keywords** scheelite, orogenic gold deposits, trace elements, cathodoluminescence, principal component analysis,

28   partial least square-discriminant analysis

Introduction

The association between gold and scheelite in orogenic gold deposits has long been recognized. Goldfarb et al. (2005) review the characteristics of orogenic gold deposits. In many deposits, scheelite predates and/or is contemporaneous with gold deposition, such as in the Val-d'Or district, Canada (Beaudoin and Pitre 2005), at Mt. Charlotte, Australia (Mueller 1991) or Charmitan, Uzbekistan (Graupner et al. 2010). Scheelite is a major mineral in greisen and skarn (Xiong et al. 2006; Ren et al. 2010; Song et al. 2014; Guo et al. 2016; Poulin 2016; Poulin et al. 2016; Poulin et al. 2018), and a minor mineral in Cu-(Mo-Au) porphyry deposits (Poulin 2016; Poulin et al. 2016; Sun and Chen 2017; Poulin et al. 2018), where it occurs in veins or disseminated in altered rocks. Scheelite is also an accessory mineral in aplite, pegmatite and metamorphosed sedimentary exhalative Fe-Mn (Brugger et al. 1998; Uspensky et al. 1998) and volcanogenic massive sulphides deposits (Poulin 2016; Poulin et al. 2016; Poulin et al. 2018).

The indicator mineral technique is used in exploration using overburden sediments for several deposit types. Discriminant geochemical features in major, minor and trace elements of indicator minerals may be used to recognize a deposit type. For instance, Cr-rich spinel and Cr-rich garnet are indicators for diamond-bearing kimberlite (Gurney 1984; Fipke et al. 1995; McClenaghan and Kjarsgaard 2007), and Ni-Cu mineralization (Aumo and Salonen 1986; Peltonen et al. 1992; Somarin 2004), whereas magnetite has been shown to be useful to fingerprint various mineral deposit types (Dupuis and Beaudoin 2011; Boutroy et al. 2014; Dare et al. 2014). Scheelite is considered an indicator mineral for orogenic gold (McClenaghan and Cabri 2011) and tungsten deposits (Lindmark 1977; Toverud 1984; Johansson et al. 1986). In indicator mineral surveys, scheelite is recovered from the heavy mineral fraction or overburden sediments, but the deposit type at the source of the scheelite grains cannot, currently, be determined.

Scheelite ($CaWO_4$) and powellite ($CaMoO_4$) form a partial solid solution where Mo^{6+} substitutes for W^{6+} (Tyson et al. 1988). Pure scheelite is bluish under short wave fluorescent light, whereas Mo-rich scheelite is typically yellow in color (Van Horn 1930; Shoji and Sasaki 1978). Scheelite is luminescent under an electron beam allowing to study textural zonation and successive scheelite generations in relationship with their trace element composition. The REE, Y, As, and Sr content in scheelite have a minor effect on the cathodoluminescence (CL) response (Brugger et al. 2000a; MacRae et al. 2009; Poulin 2016; Poulin et al. 2016), whereas Mo variation is associated with CL zoning, (Poulin 2016; Poulin et al. 2016). The CL zoning may result from primary crystallization or from multi-stage evolution (Brugger et al. 2000a).

Replacement of W by Mo and Ca by Sr, Pb, Fe, Mn, Ba and REE have been reported (Cottrant 1981; Raimbault et al. 1993; Ghaderi et al. 1999) and traces of Na, V, Nb, Ta, S, As, Pb, U, Th, Mn, Fe, Au, Ba, B, Co, Cr, K, Ni, Sb Sc, Zn, Bi,

57   Cu, Sn, Zn, Li, Ti and Rb have been measured in variable amounts in scheelite from various types of deposits (Anglin 1992;

58   Eichhorn et al. 1997; Zhigang et al. 1998; Ghaderi et al. 1999; Brugger et al. 2000a; Brugger et al. 2000b; Brugger et al. 2002;

59   Xiong et al. 2006; Liu Yan et al. 2007; Dostal et al. 2009; Graupner et al. 2010; Peng et al. 2010; Ren et al. 2010; Song et al.

60   2014; Hazarika et al. 2016; Poulin 2016; Poulin et al. 2016; Fu et al. 2017; Sun and Chen 2017).The high REE concentrations

61   (~10-5,000 ppm; Uspensky et al. 1998) in scheelite have been used for Sm-Nd geochronology in order to date the gold

62   mineralization (Anglin 1992; Anglin et al. 1996; Frei et al. 1998; Uspensky et al. 1998; Kempe et al. 2001; Roberts et al.

63   2006) whereas the Sr and Nd isotopic compositions have been used to constrain the sources and the pathway of auriferous

64   hydrothermal fluids (Bell et al. 1989; Mueller et al. 1991a; Kent et al. 1995; Darbyshire et al. 1996; Frei et al. 1998). Most of

65   the studies on Sr and Nd isotopic composition of scheelite from orogenic gold deposits conclude that the fluids are derived

66   from the mantle and/or the lower crust (Bell et al. 1989; Mueller et al. 1991a; Darbyshire et al. 1996; Voicu et al. 2000), with

67   the exception of the Muruntau gold deposit where Kempe et al. (2001) concluded that fluids were most probably derived from

68   the local host rocks. Calcium is likely derived from the regional host rocks, whereas, W is considered to be derived from the

69   hydrothermal fluids (Goldfarb and Groves 2015). Isotopic studies of scheelite have shown that Sr is partly derived from the

70   local host rocks (Mueller et al. 1991a; Darbyshire et al. 1996; Ghaderi et al. 1999; Brugger et al. 2002), whereas Pb and Nd

71   have more complex sources at the local and regional scales (Brugger et al. 2002). Poulin (2016) discriminated the trace

72   element signatures of metamorphic scheelite to that from magmatic and hydrothermal settings using the Eu anomaly vs Mo/Sr.

73   Previous studies, however, do not provide a common, comprehensive, set of minor and trace elements contents in orogenic

74   gold deposit scheelite.

75   Defining the texture, luminescence properties, and trace element composition of scheelite from orogenic gold

76   deposits could be used to identify and track these deposits in overburden sediments. In this study, we present textural and

77   chemical characteristics of scheelite from 25 orogenic gold deposits, including 13 world-class examples, that represent a large

78   variation in host rock composition and age, metamorphic facies and mineralization age, in order to characterize scheelite from

79   this deposit type. Mineral texture was investigated by CL and composition was determined by Electron Probe Micro Analyzer

80   (EPMA) for major and minor elements, and by Laser Ablation-Inductively Coupled Plasma-Mass Spectrometry (LA-ICP-

81   MS) for minor and trace elements. Discriminant binary and ternary diagrams, box plots and multivariate statistics including

82   Principal Component Analysis (PCA) and Partial Least Square-Discriminant Analysis (PLS-DA) are used to characterize

83   scheelite composition from various geological settings within the orogenic gold deposit type. Furthermore, we compare the

84   chemical composition of scheelite from orogenic gold deposits to that from other deposit types in order to define discriminant

85   criteria that would be useful to identify the source of scheelite in indicator mineral surveys.

Geological settings of the selected orogenic gold deposits

Typical samples of gold mineralization were selected from 13 world-class (Goldfarb et al. 2005) and 12 additional orogenic gold deposits and districts (ESM 1a). The set of samples is considered to represent largely the variability of orogenic gold deposit characteristics. The origin of the Kumtor, Canadian Malartic and Young Davidson deposits is still debated, but we follow Goldfarb et al. (2005) and consider they belong to the orogenic type. Mueller (1997) and Mueller et al. (2004) considered the Nevoria gold deposit as a skarn, whereas Eilu et al. (1999) and Goldfarb et al. (2005) classified it as an orogenic gold deposit. In the following, Nevoria is described with the other orogenic gold deposits. In addition, we report on the Crusader deposit that has been interpreted to be intrusion-related (Jowitt et al. 2014). Deposits were selected to provide a representative range of geological settings (ESM 1a). Host rocks consist of sedimentary (clastic, black shale, banded-iron formation), volcanic (basalt, komatiite) and plutonic rocks (syenite, granite, granodiorite, tonalite, diorite, gabbro). The selected gold deposit host rocks are metamorphosed from the lower greenschist (e.g., Paddington, Sigma-Lamaque) to the mid-amphibolite facies (e.g., Marvel Loch, Edward's Find). To simplify comparison, deposits hosted in lower greenschist facies rocks and below are labelled low metamorphic, deposits in mid-greenschist facies rocks are considered moderate metamorphic and deposits in upper greenschist to lower amphibolite facies rocks are labelled high metamorphic. Scheelite has not been described in orogenic gold deposits hosted in higher grade metamorphic rocks such as Challenger, Griffin's Find, or Renco. Most of the deposits selected formed during the Archean (e.g., Hutti) but our selection includes deposits formed during the Proterozoic (e.g., Essakane), the Paleozoic (e.g., Kumtor) and the Mesozoic (e.g., Macraes). Host rock ages range from Archean to Paleozoic (ESM 1a). In the selected deposits, scheelite occurs in the mineral assemblage of the gold mineralization.

Scheelite texture and mineral assemblages

Scheelite is commonly pinkish to whitish beige at the macroscopic scale. Scheelite occurs most commonly as centimeter-size aggregates of massive anhedral grains free of inclusions such as at Beaufor, Sigma, Dome, Canadian Malartic, Cuiaba (Fig. 1a), Essakane, Macraes, and Crusader. Scheelite locally forms isolated subhedral grains at Canadian Malartic (Fig. 1b) and Paddington. Scheelite is finely disseminated (50-500 µm) at Rosebel, Kochkar (Fig. 1d), Kumtor, Navachab, Buzwagi and Transvaal. Grain aggregates locally form veinlets at Kumtor (Fig. 1e). At Hutti, scheelite shows a polygonal fabric typical of dynamic recrystallization (Fig. 1c).

112   Mineral associations are detailed for each deposit in ESM 1b. Scheelite is most commonly associated with quartz,

113   carbonates, amphiboles, tourmaline, sericite, muscovite, feldspar, clinopyroxene, magnetite, pyrite and arsenopyrite.

114   Accessory minerals associated with scheelite are rutile, titanite, hematite, chalcopyrite and pyrrhotite. Native gold forms

115   inclusions in pyrite which is in textural equilibrium with scheelite at Paddington and Tarmoola (Fig. 1h). At Crusader, native

116   gold is in textural equilibrium with scheelite, in association with magnetite and muscovite (Fig. 1i). At Rosebel and Hutti,

117   scheelite occurs in the same sample as native gold but is not in textural equilibrium. At Norseman, coarse-grained scheelite

118   aggregates are intergrown with minor sphalerite, galena and rare native gold (Mueller 1990). All scheelite grains display

119   homogeneous blue fluorescence under UVC light, with the exception of samples from the Crusader and Nevoria deposits,

120   which exhibit a yellow colour.

121   **Analytical methods**

122   **Sample preparation**

123   Scheelite-bearing samples were collected from the selected deposits, or donated by researchers or mining companies

124   (ESM 1a). Thirty-seven polished thin sections from 25 deposits were studied using the petrographic microscope. An additional

125   five samples, from the Hollinger, Dome, Young Davidson, Sigma and Cuiaba deposits were disaggregated by Electrical Pulse

126   Disaggregation (EPD) at Overburden Drilling Management (Ottawa) to recover ultra-trace scheelite. Scheelite grains were

127   hand-picked under the binocular microscope and UVC light from the non-magnetic, heavy (SG > 3.3), 0.25-0.5 mm and 0.5-

128   1.0 mm grain size fractions. Scheelite was recovered from the EPD samples from Hollinger, Young Davidson and Sigma,

129   whereas, samples from the Dome and Cuiaba deposits contained no scheelite. Scheelite grains recovered by EPD were

130   mounted in epoxy polished sections. Scheelite grains from Marvel Loch (Mueller 1991; Mueller et al. 1991b), Nevoria

131   (Mueller 1997; Mueller et al. 2004), Edward's Find (Schwebel et al. 1995), Mount Pleasant (Cassidy and Bennett 1993), Mt.

132   Charlotte (Mueller 2015), Paddington (Hancok et al. 1990) and Norseman (Australia; Mueller 1992) were donated by A.

133   Mueller (ESM 1a) and mounted in epoxy polished section.

134   **Electron Probe Micro-Analysis (EPMA)**

135   We analysed 145 spots from 25 deposits by EPMA (ESM 2b). The major and minor element composition of scheelite was

136   measured at Université Laval using a CAMECA SX-100, equipped with five wavelength-dispersive spectrometers (WDS).

137   Major elements W and Ca were measured with a beam current of 20 nA with an accelerating voltage at 15 kV, for 20 s for

138 the peak and 10 s for the background, using a beam diameter of 10 µm. Metal tungsten (W-ATX) and diopside were used as

139 standards for W and Ca. Concentrations of Na, Sr, Mo, Y and Fe were measured with a 10 µm diameter beam with a current

140 of 100 nA, an accelerating voltage of 15 kV, and counting times of 120 s for the peak and 30 s for the background. Metal

141 molybdenum (Mo-ATX) for Mo, celestite for Sr, YPO_4 for Y, hematite for Fe and albite for Na were used as standards (ESM

142 2a). Carbonates were measured for major and minor elements including Ca, Fe, Mg, Mn and Sr using a beam diameter of 10

143 µm, a current of 20 nA and an accelerating voltage at 15 kV. Cathodoluminescence imaging was performed at 15 kV and 20

144 nA with a CAMECA cathodoluminoscope. The CL was recorded as grey-scale images to document textures and zonation in

145 scheelite.

Laser Ablation-Inductively Coupled Plasma-Mass Spectrometry (LA-ICP-MS)

147 We conducted 146 analyses, including 125 lines and 35 spots, and 7 maps from 24 deposits (ESM 2d) by LA-ICP-MS at

148 LabMaTer, Université du Québec à Chicoutimi (UQAC) using a RESOlution M-50 Excimer 193 nm laser coupled to an

149 Agilent 7700x ICP-MS with a frequency of 10 Hz and a power of 5.4 mJ.cm^{-2}. The beam size was set at 44 µm for lines and

150 spots and 33 µm for maps. Line analyses are preferred to spots for large grains. The background was counted for 30 s and the

151 acquisition time was 60 s. Scan speed was fixed at 20 mm/s for the large grains, spots and maps and 10 mm/s for grains less

152 than ca. 300 µm wide. The reference material NIST-610, NIST-612, GSD-1g-A, GSE-1g-A (Jochum et al. 2005) and

153 Gprobe6-A were used for calibration. NIST-610, GSD-1g-A and Gprobe6-A were analysed before and after a run. NIST-612

154 and GSD-1g-A were measured every hour during analytical sessions. Details for external standards are provided in ESM 2c.

155 Calcium[44] was used as the internal standard and fixed at 13.90 wt. %, based on the average EPMA composition. Data were

156 reduced using the Iolite software. Detection limits (DL) are summarized in ESM 2c.

157 Electron Probe Micro-Analysis and LA-ICP-MS analyses give the chemical composition at two different scales and

158 are therefore complementary (10 µm beam size for EPMA versus about 1000x40 µm for LA-ICP-MS line analysis). Ablation

159 lines allow to document zonation and are more representative of the bulk composition of the grain, whereas EPMA analyses

160 provide spatially resolved chemical composition. Comparison between EPMA and LA-ICP-MS data (ESM 3a) shows a good

161 correlation between the two instruments, except close to the detection limit. Scheelite does not contain inclusions at the

162 microscope scale, however, peaks in Fe-Mg-Si correlated with a sharp decrease in W and Ca in the LA-ICP-MS spectra, and

163 shows that scheelite contain locally Fe-Mg-Si-rich sub-microscopic inclusions that were excluded in data reduction.

164   **Statistical analysis**

165   Data were investigated using both basic and multivariate statistics such as Principal Component Analysis (PCA) and

166   Partial Least Square-Discriminant Analysis (PLS-DA). Electron probe microanalysis and LA-ICP-MS datasets are typically

167   censored because they contain non-detects that are below the detection limit (Helsel 2005). Censored compositional data were

168   imputed using the k-nearest neighbor function with the Aitchison distance (robCompositions package in R; Hron et al. 2010;

169   Makvandi et al. 2016b). Geochemical data, summed to 100%, can lead to spurious correlations, inherent to all compositional

170   datasets (Aitchison 1986; Whitten 1995). Data were transformed using centered-log ratio (clr; Thió-Henestrosa and Martín-

171   Fernández 2005) that is a suitable method for multivariate statistical analysis (Aitchison 1986; Egozcue et al. 2003; Makvandi

172   et al. 2016b)

173   Silica, Cr, Sn and Ag were excluded from the PCA and PLS-DA because more than 40 % of the data are below

174   detection limit (DL). Both methods plot highly positively correlated variables together in same quarter in the principal

175   components diagram, whereas, inversely correlated variables plot in opposite quarters. PCA is a non-supervised statistical

176   method that captures the maximum variance among the data set, whereas PLS-DA is a supervised statistical method of

177   classification that uses labeled data (de Iorio et al. 2007). In PLS-DA, a series of orthogonal components relate to the X (N $\times$

178   K) and Y (N $\times$ M) matrices by maximizing the covariance between the two. Loadings biplots (qw^*_1-qw^*_2) indicate the

179   correlation among different elements, and the relationship between the variables and different sample classes (e.g., host rock

180   composition). The loading values show the impact of elements on the model, and the sign of the value indicates the positive

181   or negative correlation between the elements. As a result, elements that plot in the vicinity of each other in the PLS-DA

182   loadings space show strong positive correlation, and they are inversely correlated to those in an opposite quadrant. The

183   correlation among variables and sample classes control the distribution of samples in the score scatter plot (t_1-t_2). The origin

184   of score scatter plots represents the mean composition of the whole dataset (Makvandi et al. 2016b). The Variable Importance

185   on Projection (VIP) plots are used to indicate the impact of different variables on the sample classification, where VIP values

186   equal and/or larger than 1 are the most important in the classification (Eriksson et al. 2001).

187   **Results**

188   **Cathodoluminescence and trace elements variation**

189   Scheelite from orogenic gold deposits commonly exhibits homogeneous cathodoluminescence (Fig. 2a), with brighter local

190   patches in rare samples, whereas, sub-grains can be distinguished within a larger grain (Fig. 2b). Scheelite from the Macraes

7

191   deposit consists of at least two generations: (1) a first generation that forms most of the grain, (2) younger veinlets with darker

192   CL that cut the first scheelite (Fig. 3b). The two generations of scheelite from the Macraes deposit differ in the trace element

193   composition (Fig. 3). The early, bright CL scheelite, has high Sr, Na, Mg, Mn, Th and U, and low REE and Y contents (Fig.

194   3b). The second generation of vein and breccia scheelite is darker in CL and associated with low Sr, Na, Mg, Mn, Th, and U

195   and high REE and Y contents (Fig. 3b). Dark CL breccia cuts the edge of scheelite grains from Macraes, Crusader (Fig. 2f)

196   and Mount Pleasant (Fig. 2e). Scheelite veinlets cut older scheelite at the Tarmoola deposit (Fig. 2d). Growth zoning in

197   scheelite at Kochkar (Fig. 2g) and Kumtor, where oscillatory zoning is associated with large variations in Sr, Pb, Y, Th and

198   U contents and small variations in As, Na and V. However, the small grain size (ca. 450 µm) and the narrow zones (20 to 150

199   µm) compared to the laser beam diameter (44 µm) complicate the trace element quantification of each zone. Scheelite from

200   the Crusader and Essakane deposits show both sector and oscillatory zoning under CL (Fig. 2i). The oscillatory zoning in

201   Crusader shows a dark zone with high contents in Na, V, As, Nb, REE and Y, and a low Mo, whereas, bright zones have low

202   Na, V, As, Nb, REE and Y and high Mo contents (ESM 3d). Laser ablation-ICP-MS maps of grains with homogeneous CL

203   show little-to-no variation in trace element compositions (Fig. 4).

Trace element composition

205   Strontium, Si, S and Y have median concentrations over 100 ppm, whereas, Na, Ce, Nd, Dy, Fe, Eu, Gd, Pb, Er, Sm

206   and Yb have median concentration over 10 ppm (ESM 3b). Lanthanum, K, As, Mg, Pr, Ho, Mn, Tb, Cr, Mo, Tm, Nb, Lu and

207   B have median concentration between 1 and 10 ppm. Zinc, Ba, Li, Cu, Ti, V, Sn, U, Th, Ta, Ag and Co have median

208   concentrations between 1 and 0.01 ppm. More than 40% of Si, Cr, Sn, Cr and Ag analyses are below detection.

Rare earth elements and yttrium

210   Rare Earth Element (REE) patterns for each deposit are shown in ESM 3e and f. Rare earth elements display five

211   patterns with a scheelite/chondrite ratio from 0.2 to 4000, but most are near 100 (Fig. 5): 1) a bell-shaped pattern with a

212   positive (Fig. 5a) or 2) a negative Eu anomaly (Fig. 5c); 3) a flat pattern with a positive Eu anomaly (Fig. 5b); 4) a LREE

213   enriched pattern with small positive to no Eu anomaly (Fig. 5d) and 5) a HREE enriched pattern with positive to no Eu

214   anomaly (Fig. 5e). Rare earth elements normalized to the North American Shale Composite (NASC; Fig. 5; Gromet et al.

215   1984) show a ratio varying from 1 to 100 order of magnitude. Few analyses show a weak depletion in Middle REE (MREE)

216   that are marginally distinct from the flat pattern and, are here included with the flat pattern group in this description (ESM

217   3e). Most scheelite grains show a single REE pattern (ESM 3e and f). The bell-shaped and flat patterns represents, 33 % and

218   40 % of the analyses, respectively. Scheelite from Paddington, Tarmoola, Norseman, Mt. Charlotte and Macraes, displays

8

219   both bell-shaped and flat patterns with positive Eu anomalies (ESM 3e and f). In the Macraes deposit, early scheelite has a

220   flat pattern, whereas, the later breccia scheelite shows a bell-shaped pattern, both with a positive Eu anomaly (Fig. 3c).

221   Scheelite from deposits hosted in low metamorphic facies rocks commonly present positive Eu anomalies (Essakane,

222   Paddington, Macraes; ESM 3e and f). Several deposits hosted in moderate to high metamorphic grade rocks show strong

223   variations of Eu anomalies, such as Tarmoola, Norseman, Mt. Charlotte (ESM 3f).

224   The LREE-enriched pattern is found in scheelite from the Young Davidson, Kochkar and Kumtor deposits (Fig. 5;

225   ESM 3e). Kochkar scheelite is associated with calcite and has a lower REE content than scheelite in samples free of carbonates

226   (ESM 3c and e). However, both have similar LREE-enriched pattern (ESM 3e). Scheelite from Young Davidson and Canadian

227   Malartic have a LREE-enriched pattern in addition to the more common bell-shaped pattern (ESM 3e). The LREE-enriched

228   pattern has a shape similar to that of NASC (Fig. 5d). Scheelite from the Crusader deposit and the Type-II scheelite at Hutti

229   (Hazarika et al. 2016) have HREE-enriched patterns (Fig. 5e; ESM 3e). The REE pattern of scheelite from the Crusader

230   deposit is similar in both CL zones (ESM 3d). Scheelite from Nevoria exhibits a REE pattern different from that of other

231   orogenic gold deposits, with a flat REE pattern and a scheelite/chondrite ratio of about 10 and no Eu anomaly (Fig. 5f).

232   Binary plots of $(La/Sm)_{CN}$ vs. $(Gd/Yb)_{CN}$ allows easy comparison of LREE- and HREE-enrichment patterns (Fig.

233   6a). Scheelite from orogenic gold deposits plots along a line with a negative slope in that diagram. Scheelite with bell-shaped

234   REE patterns and negative Eu anomaly have low $(La/Sm)_{CN}$ (median 0.03) and high $(Gd/Yb)_{CN}$ (median 10) . Scheelite with

235   bell-shaped REE patterns with a positive Eu anomaly have intermediate $(La/Sm)_{CN}$ (median 0.2) and high $(Gd/Yb)_{CN}$ (~ 5) .

236   Scheelite with a flat REE pattern has $(La/Sm)_{CN}$ and $(Gd/Yb)_{CN}$ ratios near 1 (median 0.9 and 1, respectively). Scheelite with

237   HREE-enriched patterns has low $(La/Sm)_{CN}$ (median 0.12) and $(Gd/Yb)_{CN}$ (median 1.6) , whereas, scheelite with LREE-

238   enriched patterns has high $(La/Sm)_{CN}$ (median 1) and $(Gd/Yb)_{CN}$ (median 10; Fig. 6a). REE patterns with a negative Eu

239   anomaly are characterized by high Na content (median 156 ppm; Fig. 7b).

240   Yttrium concentration ranges from 2.14 to 1680 ppm. Yttrium displays a correlation with the REE (Fig. 7h). Scheelite

241   from deposits formed during the Archean, Proterozoic and Phanerozoic have comparable ∑REE and Y contents (Fig. 7h).

242   Scheelite from deposits hosted in felsic to intermediate rocks have high ∑REE (median 645 ppm and 1164 ppm, respectively)

243   and Y contents (median 348 ppm and 605 ppm, respectively), whereas, scheelite from deposits hosted in sedimentary rocks

244   have lower ∑REE (median 195 ppm) and Y contents (median 113 ppm). Scheelite from deposits hosted in mafic to ultramafic

245   rocks overlap the scheelite composition from deposits hosted in felsic to intermediate rocks, and in sedimentary rocks (∑REE:

246   5-3900 ppm and Y: 5-1700 ppm; Fig. 7h). The Eu anomaly is typically negative or close to zero for scheelite hosted in felsic

247   to intermediate composition rocks (Fig. 7b). Scheelite from deposits in low and moderate metamorphic grade rocks have

9

248 higher ∑REE (median 334 ppm and 632 ppm, respectively) and Y (median 145 ppm and 253 ppm, respectively) contents

249 compared to scheelite from deposits in high metamorphic grade rocks (median ∑REE 101 ppm and Y 37 ppm; Fig. 7h).

250 **Strontium and lead**

251 Strontium in scheelite from orogenic gold deposits ranges from 83 to 7300 ppm, with a mean of 1244 ppm and a

252 median of 653 ppm (Fig. 8a). The EPMA concentrations for Sr are commonly lower than the LA-ICP-MS values when

253 approaching the EPMA detection limit (ESM 3a). Scheelite from Phanerozoic sedimentary host rocks has higher Sr

254 concentrations (median 3160 ppm) than those from Proterozoic and Archean host rocks (median 2478 ppm and 576 ppm

255 respectively; Fig. 7d and e). Scheelite from deposits hosted in sedimentary and felsic rocks has high Sr contents (median 2890

256 ppm and 811 ppm, respectively) compared to deposits hosted in mafic and ultramafic rocks (median 548 ppm). Scheelite

257 hosted in low and moderate metamorphic grade rocks have Sr contents (median 661 ppm and 1278 ppm, respectively), higher

258 than those hosted in higher metamorphic grade rocks (median 442 ppm; Fig. 7d). Scheelite from Crusader has low Sr

259 concentrations compared to scheelite from the other deposits studied (median 121 ppm). Strontium and Pb data show a positive

260 correlation (Fig. 7f), such that scheelite Pb composition similarly varies with the metamorphic grade of the host rocks, except

261 for Macraes deposit which has low Pb concentrations (median 6 ppm) compared to other low metamorphic grade sedimentary

262 rock hosted deposits (median 28 ppm). The binary diagram ∑REE+Y vs. Sr (Fig. 7d) allows the discrimination of scheelite

263 from low and moderate metamorphic facies host rocks, which typically have higher ∑REE+Y and Sr contents, than scheelite

264 hosted in high metamorphic grade rocks.

265 **Molybdenum**

266 Molybdenum concentrations in scheelite from orogenic gold deposits does not vary significantly in terms of host

267 rock composition, metamorphic grade and age of mineralization. High Mo scheelite from Crusader and Nevoria display a

268 yellow colour under UVC light (median 6.3 wt % and 1.3 wt % Mo, respectively; Fig. 8b). Scheelite from the Canadian

269 Malartic, Kochkar and Kumtor deposits has a relatively high Mo content and are more whitish under UVC light, (median

270 1395 ppm; 383 ppm and 203 ppm, respectively, ESM 2b and d).

271 **Sodium**

272 Sodium concentrations by EPMA and LA-ICP-MS covary moderately (R^2=0.37; ESM 3a). EPMA data for Na are

273 commonly higher than LA-ICP-MS data (Fig. 8) perhaps due to sample heterogeneity at the scale of the laser beam spot, as

274 reference material monitoring is good and Na varies in zoned scheelite. Sodium concentration by LA-ICP-MS is highly

275 variable in scheelite from Kochkar ($\bar{x}$ =133 ± 256 ppm; n=19) and in scheelite from Beaufor ($\bar{x}$ =183 ± 94 ppm; n=23).

276   Sodium shows a positive correlation with $\sum$REE+Y (Fig. 7a), and a negative correlation with the Eu anomaly (Fig. 7b). The

277   Na content is higher in scheelite from deposits hosted in felsic to intermediate rocks (median 120 ppm and 194 ppm,

278   respectively), and lower in deposits hosted in sedimentary rocks (median 53 ppm). Sodium in scheelite from deposits hosted

279   in mafic to ultramafic rocks plots across the range of Na values (4-379 ppm; Fig. 7e).

280   **Vanadium, niobium, tantalum and arsenic**

281   Vanadium, Nb, Ta and As have low concentration in scheelite from orogenic gold deposits with medians of 0.42 ppm, 8.41

282   ppm, 0.13 ppm and 11 ppm, respectively. At Crusader, V, Nb, Ta and As are higher in concentration in the dark CL zone

283   compared to the lighter CL zone (ESM 3d). Niobium and Ta show a positive correlation in all deposits (Fig. 7c).

284   Niobium+Ta+V contents display a positive covariation with REE+Y, forming two broad sub-parallel arrays, with an array for

285   deposits hosted in low and moderate metamorphic facies rocks at lower Na+Ta+V values compared to deposits hosted in high

286   metamorphic facies rocks. In the binary diagram (Sr+Na) / (Sr+Na+10x(Nb+Ta+V+As)) vs. ((REE+Y)+10x(Nb+Ta+V+As))

287   / (Sr+(REE+Y)+10x(Nb+Ta+V+As)), scheelite from deposits hosted in low to moderate metamorphic facies rocks plots along

288   a vertical trend at (Sr+Na)/(Sr+Na+10x(Nb+Ta+V+As)) ~ 1 (Fig. 9a). Scheelite from deposits hosted in rocks at high

289   metamorphic grade plot typically along a curve from upper left to lower right corners of the diagram (Fig. 9a).

290   **Magnesium, manganese and iron**

291   Correlated peaks in Mg, Mn and Fe, that do not show peaks in Si and S, in LA-ICP-MS spectra indicate

292   submicroscopic inclusions, perhaps oxides. Other inclusions contain Si or S suggesting silicates and sulfides. In scheelite, Mg

293   and Fe are highly correlated (r^2= 1), whereas, Mn shows wide covariation with Mg or Fe. Scheelite from deposits hosted in

294   clastic sedimentary rocks has higher Fe and Mg concentrations (~ 29 ppm and ~ 14.8 ppm, respectively) than scheelite from

295   deposits hosted felsic to intermediate rocks (median Fe 23 ppm and 22 ppm, respectively; median Mg 5 ppm and 8 ppm).

296   Iron, Mg and Mn contents are not distinctive for deposits hosted in mafic to ultramafic rocks. The ternary Fe-Mn-Mg diagram

297   (Fig. 9b) shows that scheelite from deposits hosted in low to moderate metamorphic facies rocks have higher Mg, Fe and Mn

298   contents (median Mg 6.5 ppm and 8.6 ppm, respectively; median Fe 27.7 ppm and 26.4 ppm, respectively; median Mn 2.9

299   ppm and 3.4 ppm, respectively), compared to scheelite in deposits hosted in high metamorphic facies rocks (5.4 ppm, ~ 22

300   ppm and 9 ppm, respectively; Fig. 9b). A similar distribution of Fe-Mn-Mg is found for carbonates associated with scheelite,

301   with the exception of the high metamorphic facies Transvaal deposit, which has low Mn and high Mg (Fig. 9c).

302   **Uranium and thorium**

303   Scheelite from deposits hosted in Proterozoic and Phanerozoic rocks have higher Th (median 0.94 ppm and 0.85

304   ppm, respectively) and U (median 4.87 ppm and 1.21 ppm, respectively) concentrations compared to scheelite from deposits

305   hosted in Archean rocks (median Th 0.02 ppm and U 0.02 ppm; Fig. 7i). Thorium and U contents are higher in scheelite from

306   deposits hosted in sedimentary rocks (median 0.88 ppm and 1.8 ppm, respectively), and lower in scheelite from deposits

307   hosted in intermediate plutonic rocks (median 0.01 ppm and 0.01 ppm, respectively). Scheelite from Kochkar has the highest

308   concentrations in Th and U (median 0.98 ppm and 0.6 ppm, respectively). Scheelite from deposits hosted in mafic to ultramafic

309   rocks have Th and U concentrations similar to values for the other deposits (0-1.50 ppm and 0-8.90 ppm, respectively). There

310   is no systematic change in U and Th contents with increasing metamorphic grade of host rocks.

311   **Multivariate statistics of scheelite trace element composition**

312   Principal Component Analysis and PLS-DA of scheelite LA-ICP-MS data (Na, Mg, S, Ti, V, Mn, Fe, Co, As, Sr, Y, Nb, Mo,

313   Ba, ∑REE, Eu anomaly (Eu*), Ta, Pb, Th and U) for orogenic gold deposits are used to investigate the relations between

314   composition and age of mineralization, host rock composition, and metamorphic facies of the host rocks (Fig. 10 and ESM

315   3g). Scheelite from Nevoria has controversial affinity and a trace element composition different to that from the other orogenic

316   gold deposits. For this reason, scheelite from Nevoria is not included from the PLS-DA (Fig. 10). The REE suite has been

317   reduced to ∑REE to facilitate the discussion and emphasize other trace element variations without changing the PCA and

318   PLS-DA results significantly. Data from the Crusader deposit were excluded from both analyses because of its controversial

319   origin, and because it has distinct geochemical features compared to the other orogenic gold deposits. The principal

320   components PC1, PC2 and PC3 represent 20.4 %, 14.1 % and 10.2 %, respectively, of the total variance of the dataset (ESM

321   3g). PC1 is defined by positive contributions of Nb, ∑REE, Y, As, Ta, V and Na (loading > 0.2) and negative contributions

322   of Eu*, Sr, U, Th, Fe, Mg and Ba (loading < -0.2), in decreasing order of importance. PC2 is defined by positive contributions

323   of K, Na, Cu, Zn, Pb, ∑REE, B and Y (loading > 0.2) and negative contributions of Th, U and As (loading < -0.2). PC3 is

324   defined by positive contributions of Mn, Eu*, S, K, Ta and Zn (loading > 0.2) and negative contributions of ∑REE, Mg, Ti,

325   Co, Y and Na (loading < -0.2). In PC1-PC2 and PC1-PC3 spaces (ESM 3g), scheelite from deposits formed during the

326   Proterozoic and Phanerozoic, with the exception of Meliadine (Canada), forms two groups, both with negative PC1 scores.

327   Scheelite from Proterozoic deposits has PC2 and PC3 scores close to 0, whereas, those from Phanerozoic deposits has negative

328   PC2 and PC3 scores. In PC2-PC3 space (ESM 3g), scheelite from Meliadine plots with the Proterozoic deposits, forming a

329   steep array. Scheelite from Archean deposits overlap with that from Proterozoic and Phanerozoic deposits in PC1-PC2, PC1-

330   PC3 and PC2-PC3 spaces (ESM 3g). PLS-DA classifies scheelite by age of mineralization (Fig. 10a and b). Archean deposits

331 are characterized by positive t_1 (positive contributions of Cu, Y, Na and $\sum$REE) and Proterozoic deposits by negative t_1 and

332 t_2 values (negative contributions of Pb, Zn, Eu*, U), whereas, Phanerozoic deposits have negative t_1 and positive t_2 values

333 (positive contributions of Ba, Mo, As, Mg).

334   Scheelite from deposits hosted in sedimentary rocks have negative PC1 scores, and PC2 and PC3 scores near 0 (ESM

335 3g). Scheelite from deposits hosted in felsic to intermediate rocks, with the exception of Kochkar, have positive PC1, positive

336 PC2, and slightly negative PC3 scores. Scheelite from deposits hosted in felsic to intermediate rocks, with the exception of

337 Kochkar, form an array distinct from that of scheelite from deposits hosted in sedimentary rocks in PC1-PC2 and PC1-PC3

338 (ESM 3g). Scheelite from deposits hosted in mafic to ultramafic rocks overlap with that from deposits hosted in sedimentary

339 and felsic to intermediate rocks in PC1-PC2, PC1-PC3 and PC2-PC3 spaces (ESM 3g). PLS-DA yields marginally improved

340 classification of orogenic gold deposit scheelite according to the composition of the host rocks (Fig. 10c and d). Deposits

341 hosted by ultramafic and mafic rocks overlap slightly with deposits hosted in intermediate rocks and mainly with deposits

342 hosted in sedimentary rocks. Deposits hosted by ultramafic and mafic rocks have low t_2 values, defined by Zn, K, S, Eu*, Fe,

343 B and Cu, whereas, deposits hosted by felsic and sedimentary rocks with positive t_1 values (Mo, Th, V, As; Fig. 10d). Deposits

344 hosted by rocks of intermediate compositions are well classified with negative t_1 values defined by Cu, Y, Na, $\sum$REE and Mo

345 (Fig. 10c and d).

346   Scheelite from deposits hosted in low and moderate metamorphic grades rocks have positive to negative PC1, mostly

347 positive PC2, and negative PC3 scores. Scheelite from deposits hosted in high grade metamorphic rocks have positive to

348 negative PC1, mostly negative PC2, and positive PC3 scores. Thus, scheelite from deposits hosted in low and moderate

349 metamorphic grades rocks form a group that partly overlaps with scheelite from deposits in high grade metamorphic rocks in

350 PC2-PC3 space (ESM 3g). Classification of scheelite according to the metamorphic grade of the host rocks by PLS-DA yields

351 well separated deposits hosted by high grade metamorphic rocks with positive t_1 values defined by Mn, As, Nb and Ta (Fig.

352 10e and f). Deposits in low grade metamorphic rocks have negative t_1 and t_2 values (Eu*, U, S, Th), whereas, deposits hosted

353 in intermediate grade metamorphic rocks with low t_1 values are not classified by t_2, overlapping with deposits hosted in low

354 grade metamorphic rocks with negative t_2 (Fig. 10e and f).

Discussion

Trace element substitution

Cation substitution in scheelite has been discussed for minor elements (Nassau 1963; Nassau and Loiacono 1963; Cottrant 1981; Burt 1989; Raimbault et al. 1993; Brugger et al. 2002; Brugger et al. 2008). Brugger et al. (2008) developed a formal thermodynamic analysis of the controls on Eu^{2+}/Eu^{3+} uptake by hydrothermal scheelite. Rare Earth Elements are common in concentrations between 10-5000 ppm in scheelite (Uspensky et al. 1998) and substitute in the Ca site (Raimbault et al. 1993):

$$3Ca^{2+} = 2REE^{3+} + \square Ca \qquad (Eq.\ 1)$$

The substitution can also be coupled either with Na or Nb to balance the charges (Nassau 1963; Burt 1989; Brugger et al. 2002):

$$2Ca^{2+} = (REE,Y)^{3+} + Na^+ \qquad (Eq.\ 2)$$
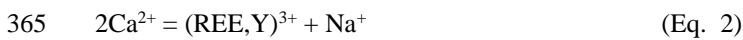
The correlation between $\sum REE+Y$ and Na (Fig. 7a) is indicative of the coupled substitution mentioned in Eq. 2 (Nassau 1963; Nassau and Loiacono 1963; Cottrant 1981; Burt 1989; Raimbault et al. 1993; Brugger et al. 2002). The coupled substitution from Eq. 2 is considered a major substitution in scheelite (Nassau and Loiacono 1963; Cottrant 1981; Burt 1989; Raimbault et al. 1993; Brugger et al. 2002).

Octohedral 6-coordinated Ta (V) and V (V) have similar radius (Ta: 78 pm, V: 68 pm) to Nb (78 pm). This, combined with the positive correlation between $\sum REE+Y$ and Nb+Ta+V (Fig. 7g) and Eq. 2, suggest that Ta and V may substitute for W in the following coupled substitution such as:

$$Ca^{2+} + W^{6+} = REE^{3+} + (Nb, Ta, V)^{5+} \qquad (Eq.\ 3)$$
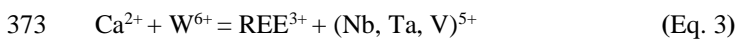
The ionic radius of some elements, such as Fe (II, 106 pm), Pb (II, 143 pm) and Mn (II, 110 pm) differ by less than 15 %, in 8-coordination, with that of ionic radius of Ca (II) of 126 pm. This suggests that the following substitutions are permissive:

$$Ca^{2+} \leftrightarrow Eu^{2+}, Sr^{2+}, Fe^{2+}, Pb^{2+}\ or\ Mn^{2+} \qquad (Eq.\ 4)$$
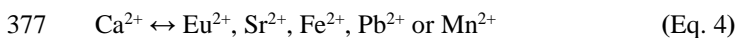
In contrast Ba (II, 156 pm) and Mg (II, 103 pm) have more than 15 % difference with Ca^{2+} 8-coordination ionic radius, which perhaps explains the low Ba content in scheelite.

14

380   The trace element composition of scheelite depends on several factors including the hydrothermal fluid composition,

381   host rock composition, temperature, pressure, pH and Eh, as well as, the partition coefficients between fluid, scheelite, and

382   co-precipitating minerals. The auriferous hydrothermal fluids forming orogenic gold deposits are mixed aqueous-carbonic

383   fluid with a low salinity with a low variance in composition (Goldfarb et al. 2005). Garofalo et al. (2014) showed that the

384   fluids contain Na, subordinate K and B, and minor amounts of trace elements including Cu, As, Li, Sr, Rb, Ba, Cs, Sb and

385   Au. Calcium is absent on this list, consistent with fluid inclusion data as reviewed in Goldfarb et al. (2005), and despite

386   common formation of calcium carbonates (calcite, ankerite) and tungstate (scheelite) in the veins. The low variance in

387   hydrothermal orogenic gold deposit fluid compositions is in contrast to the variations measured in the trace element

388   composition of scheelite, which varies with the metamorphic facies and the host rock composition (Fig. 7, 9 and 10).

389   Manganese concentration in scheelite is lower in low to moderate grade metamorphic rocks, whereas it is higher in

390   deposits hosted in high grade metamorphic rocks (Fig. 9b, 10e). A similar trend is observed for Mn concentrations in

391   carbonates: low to moderate Mn concentration is characteristic for deposits in low and moderate grade metamorphic rocks,

392   whereas moderate to high Mn concentrations are typical for deposits hosted in high grade metamorphic rocks, with the

393   exception of Transvaal (Fig. 9c; ESM 3c). An experimental study of phase transitions of Ca-Mn carbonates by Shi et al.

394   (2012) shows an increase in concentration of $MnCO_3$ in carbonates with increased pressure, which is consistent with the Mn-

395   rich carbonates in deposits hosted by high grade metamorphic rocks (Fig. 9c). We suggest that the increased Mn contents in

396   scheelite hosted in high grade metamorphic rocks, similarly, may be pressure-related.

397   **Age and host rock composition**

398   The progressive increase of Sr concentration in scheelite from deposits formed during the Archean to the Phanerozoic

399   (Fig. 7d and e) mimics the enrichment in Sr in shales during the Earth cratonization (Condie 1993). Thus, it is likely that the

400   Sr content in scheelite is largely inherited from Sr concentrations in the host rocks. This result corroborates with those of

401   Brugger et al. (2002) who showed that Sr in scheelite from the Mt. Charlotte orogenic gold deposit is partly derived from the

402   felsic units in the host rocks. Brugger et al. (2002) also suggested that Mt. Charlotte scheelite Nd and Pb were derived either

403   locally or regionally from the greenstone belt host rocks. Scheelite from deposits hosted in sedimentary rocks commonly has

404   high concentrations in Pb, U and Th, also shown by Scanlan et al. (2018), compared to scheelite from deposits hosted in other

405   rock types (Fig. 7f and i). Shales commonly have high Pb, U and Th compared to other rock types (Condie 1993), which

406   suggests that a Pb, U and Th signature in scheelite is also inherited from the sedimentary host rocks. This corroborates the

407   results of Mortensen et al. (2010) who showed the Pb isotope compositions of sulfides are similar to those from the

408   sedimentary rocks that host the gold mineralization in the Otago Schist (New Zealand). Scheelite from deposits hosted in

409 sedimentary and felsic to intermediate rocks, with the exception of Kochkar, plot as two groups in PC1-PC2 and PC1-PC3

410 spaces (ESM 3g), and in t_1-t_2 (Fig. 10d), indicating that the host rock compositions exert a control on the fluid trace element

411 composition, likely as a result of the reaction and exchange between hydrothermal fluids and host rocks, a well-documented

412 process (Ridley and Diamond 2000; Goldfarb et al. 2005; Goldfarb and Groves 2015). Overlap of scheelite compositions,

413 classified by host rock types (Fig. 10d), likely reflects the complex lithological packages hosting the deposits, compared to

414 the simplified lithological classification used in our PLS-DA. For example, the Cuiaba deposit is attributed to the mafic

415 volcanic host rock class because this is the dominant lithology, but the lithological package also comprises Fe-carbonate facies

416 BIF, perhaps explaining the PC1-PC2 scores overlapping the sedimentary and mafic volcanic class fields (ESM 3g). The

417 Meliadine deposit represents an interesting case documenting the influence of the host rock composition on the geochemistry

418 of scheelite. Meliadine is hosted by Archean rocks, but mineralization is Proterozoic in age (Lawley et al. 2015). This could

419 explain why Meliadine scheelite plots with Archean deposits in PC1-PC2 space (ESM 3g) and when projected on t_1-t_2 (Fig.

420 10b), thus suggesting that the composition is determined, at least in part, by secular change in composition of the cratonic

421 host rocks.

422   Chemical elements that are important in classification of orogenic gold deposits by dominant host rock lithology

423 likely were leached by hydrothermal fluids from the regional country rocks. These elements (Fig. 10) are Sr, Ba Th, U in

424 sedimentary rock-hosted, Mo in felsic rock-hosted, Cu, Na, ∑REE, Y in intermediate rock-hosted, and Eu*, Fe, K, S, Zn in

425 mafic rock-hosted deposits, whereas ultramafic-rock hosted deposits plot near the origin of the loadings biplot indicating

426 lesser quality classification (Fig. 10c). In contrast, some elements (Co, Mg, Pb, Ti) consistently have low VIP values in

427 classifying orogenic gold deposits with respect to the dominant host rock lithology. Some of these elements (Co, Ti) have a

428 low solubility in hydrothermal fluids and their concentrations could be less modified by exchange with the country rocks, but

429 this is not the case for Mg and Pb, as shown by the variation in Pb isotope composition in scheelite (Brugger et al. 2002).

430   **REE patterns**

431 A comparison of scheelite REE patterns with those of the host rocks from the deposits (ESM 3e and f) shows no systematic

432 trend. This is in agreement with Brugger et al. (2000b) and Brugger et al. (2002) who showed that scheelite exerts a strong

433 crystallographic control on the REE incorporation. Brugger et al. (2008) advocated closed-system crystallization of scheelite

434 to explain the change in REE patterns at Mt. Charlotte. The various REE patterns in orogenic gold deposits are not commonly

435 found in the same grains, such that a closed-system process is not applicable to most scheelite from orogenic gold deposits.

436 Scheelite has REE patterns similar to those of the country rocks at Kochkar, Kumtor, Hollinger and Mt. Charlotte (Kerrich

and Fryer 1978; Condie 1993; Kolb et al. 2005; Mueller 2015), which may indicate a local source for the REE, or that the

host rocks are equivalents of the source rocks, but just at different crustal depths. In other deposits (Meliadine, Sigma,

Lamaque, Young Davidson, and Crusader), scheelite REE patterns differ from those of host rocks, perhaps indicating that the

REE signature was not acquired by simple exchange with local country rocks for which the REE patterns are known. The

various REE patterns in scheelite do not correlate with the metamorphic grade of the host rocks, consistent with lack of change

of REE patterns of rocks during prograde metamorphism (Spandler et al. 2003). The range of REE patterns in scheelite

suggests that REE fluid-scheelite partitioning is not the dominant process controlling scheelite composition, but, instead, that

the REE patterns are controlled by the composition of hydrothermal fluids (Sylvester and Ghaderi 1997; Ghaderi et al. 1999;

Brugger et al. 2000b; Dostal et al. 2009; Peng et al. 2010; Song et al. 2014) and, perhaps, the partition coefficient of co-

precipitating minerals, although we do not have adequate data to discuss this hypothesis. For instance, Song et al. (2014) and

Zhao et al. (2018) assumed, based on the HREE enriched patterns in garnet and amphibole, that the LREE enriched patterns

in skarn scheelite resulted from crystallization garnet and amphibole, which left the residual fluid depleted in HREE.

Similarly, Cave et al. (2016) suggested that early crystallization of epidote, titanite and apatite, which have LREE enriched

patterns, may be responsible for the HREE enriched patterns in syn-metamorphic scheelite from the orogenic gold deposits

of the Otago Schist (New Zealand). The fact that the gold-bearing hydrothermal fluids display limited compositional variation

between orogenic gold provinces (Goldfarb et al. 2005), suggests that the variation in REE patterns in scheelite reflects the

sources of hydrothermal fluids with some modifications by reaction with the deposit country rocks.

The flat and bell-shaped patterns have previously recognized at Drysdale, Mt. Charlotte (Brugger et al. 2000a;

Brugger et al. 2000b), Björkdal (Roberts et al. 2006), and the Kambalda and Norseman districts (Ghaderi et al. 1999). Both

patterns are found in several additional orogenic gold deposits, which suggests similar fluid sources or similar fluid

compositions (ESM 3e and f). Several studies showed that scheelite from orogenic-gold deposits can exhibit two REE patterns

in one grain, more commonly evolving from a bell-shaped pattern to a flat and MREE-depleted pattern, with positive Eu

anomalies (Sylvester and Ghaderi, 1997; Ghaderi et al., 1999; Brugger et al., 2000). Brugger et al. (2000a; 2002) showed that

subtle CL zoning in Mt. Charlotte scheelite correlates with a change from a bell-shaped to a flat REE pattern and interpreted

that change as varying amounts of REE fractionated by scheelite crystallisation in closed system reflecting the dynamics of

the hydrothermal system. A change in REE patterns from flat to bell-shaped, associated with CL zoning, is also documented

at Macraes and Mt Pleasant (Fig. 2e and 3). The flat and bell-shaped REE patterns are commonly found in the same deposit

or in the same scheelite grain (Fig. 5 and ESM 3e and f). At Macraes, the flat pattern predates the bell-shaped pattern, which

465   suggests a change in fluid composition between the two scheelite stages (Dostal et al. 2009; Ghaderi et al. 1999; Brugger et

466   al. 2000b).

467   Scheelite in the Kochkar, Kumtor and Muruntau (first generation scheelite, Kempe et al. 2001) orogenic gold deposits

468   have LREE-enriched patterns, and yet are hosted in different rock types in different tectonic terranes (Mao et al. 2004; Kolb

469   et al. 2005). The scheelite REE patterns from each of these deposit share similarities with the REE pattern of their respective

470   host rock (ESM 3e and f; Kempe et al. 2001). The Kumtor scheelite REE pattern, hosted in carbonaceaous phyllite and

471   diamictite (Mao et al. 2004) is similar to those of Phanerozoic shales (ESM 3e; Condie 1993). Based on Sr, Sm and Nd isotope

472   compositions at Muruntau, Kempe et al. (2001) concluded that the most probable source of Sr and Nd in both generations of

473   scheelite (LREE-enriched and bell-shaped patterns) was from the metasedimentary host rocks through intensive fluid-rock

474   exchange.

475   The Crusader and Hutti deposits have HREE-enriched patterns (Fig. 5e) similar to that of syn-metamorphic scheelite

476   from the Otago schist (Type-A scheelite; Cave et al. 2016). The positive-slope REE pattern at Hutti (Type II in stage 2

477   scheelite) has been interpreted to be derived from a different hydrothermal event, at a different temperature and pressure, than

478   scheelite with the bell-shape pattern (Hazarika et al. 2016). Cave et al. (2016) explained the Otago schists scheelite HREE-

479   enriched patterns by partitioning of LREE in the co-precipitating Ca-rich silicates.

480   **Eu anomaly**

481   The incorporation of REE^{3+} in scheelite is controlled by coupled substitutions, whereas Eu^{2+} can substitute directly

482   for Ca in scheelite (eq. 4; Nassau 1963; Nassau and Loiacono 1963; Cottrant 1981; Burt 1989; Raimbault et al. 1993; Ghaderi

483   et al. 1999; Brugger et al. 2008). The most important factors controlling the Eu anomaly include: initial Eu^{2+}/Eu^{3+} ratio in

484   hydrothermal fluid, redox state, temperature, as well as the relative abundance of sites for Eu^{2+} and Eu^{3+} substitution in the

485   structure of scheelite (Ghaderi et al. 1999). High abundance of Eu^{2+} may also derive from feldspar alteration by hydrothermal

486   fluids (Alderton et al. 1980).

487   Strong positive Eu anomalies are predominantly associated with flat REE patterns that have low ∑REE content,

488   whereas, weak positive to negative Eu anomalies are characteristic of scheelite with higher ∑REE content (Fig. 5 and 6b).

489   Similar to Ghaderi et al. (1999), some deposits hosted in greenschist facies rocks display small variations of the magnitude of

490   the positive Eu anomaly associated with a variation in the concentrations of the other REE (e.g. Essakane, Paddington,

491   Macraes; ESM 3e and f). However, some deposits hosted in moderate to high grade metamorphic rocks show large variations

492   of the size of the Eu anomaly associated with small variations of Eu concentrations (e.g. Tarmoola, Marvel Loch, Norseman,

493   Mt. Charlotte; ESM 3f). In the Kalgoorlie-Norseman region, Ghaderi et al. (1999) proposed that at greenschist facies, high

494 Na activity was caused by buffering of the fluids by mafic rocks, whereas low Na activity is characteristic of high metamorphic

495 grades. However, as shown on Figure 7b, the increase in scheelite Na concentrations correlates with a change from a strong

496 positive to a negative Eu anomaly, but it does not correlate with a change in metamorphic grade. The high Na concentration

497 associated with negative Eu anomaly in scheelite is characteristic of deposits hosted by felsic to intermediate host rocks (Fig.

498 7b; e.g. Young Davidson, Beaufor, Sigma, Lamaque, Canadian Malartic), which suggests that high Na concentrations in

499 hydrothermal fluids precipitating scheelite may be due to fluid exchange with Eu-poor albite.

500   Based on the metamorphic grade of host rocks, and estimated P-T conditions of gold mineralization (ESM 1), Eu

501 should occur predominantly in the divalent state (>250°C, Sverjensky 1984;Liu et al. 2017) in deposits hosted in moderate

502 and high grade metamorphic rocks. However, the P-T conditions of hydrothermal fluids from which scheelite crystallized are

503 not well constrained for all the studied deposits. Therefore, Eu^{3+} may be dominant in deposits formed at the lower end of

504 temperatures recorded for orogenic gold deposits. In addition, Brugger et al. (2008) showed that the Eu^{2+}/Eu^{3+} ratio is

505 controlled by pH, whereas, Liu et al. (2017) showed the aqueous species have a significant impact on the oxydation state of

506 Eu in hydrothermal fluids. As mentioned above, various mechanisms such as direct substitution of Eu^{2+} for Ca and coupled

507 substitutions of Eu^{3+} may also affect Eu^{3+}/Eu^{2+} ratios in REE patterns of scheelite. In addition to the temperature dependence

508 of Eu^{3+}/Eu^{2+} ratios (Sverjensky 1984), high Na concentrations associated with variations in the Eu anomaly (Fig. 7b), support

509 the work of Brugger et al. (2008) that suggested the coupled substitution $2Ca^{2+} = REE^{3+} + Na^+$ plays an important role

510 controlling REE^{3+} substitution during scheelite crystallization from hydrothermal fluids.

511 **Comparison to scheelite from other types of deposits**

512 **Trace element composition**

513   Previous studies show that scheelite from several orogenic gold deposit have similar $(Gd/Yb)_{CN}$ and $(La/Sm)_{CN}$ ratios

514 (Fig. 6a) and similar $\sum REE$ and Eu anomaly (Fig. 6b) to those reported in our study. Scheelite from other gold, porphyry-

515 related, breccia, greisen, skarn and polymetallic vein deposits have similar $(Gd/Yb)_{CN}$ and $(La/Sm)_{CN}$ ratios (Fig. 6c) and

516 similar $\sum REE$ and Eu anomaly (Fig. 6d) compared to scheelite from orogenic gold deposits. Thus, the REE patterns including

517 the $(Gd/Yb)_{CN}$ and $(La/Sm)_{CN}$ ratios, $\sum REE$ and the Eu anomaly do not discriminate orogenic gold deposit scheelite from that

518 from other types of deposits. Scheelite from orogenic gold deposits commonly have high Sr content, high Sr/Mo ratio, large

519 Eu anomaly, and low Mo and As contents compared to scheelite from other deposit types (Fig. 11), such that Sr, Mo, and As,

520 combined with the Eu anomaly are useful to distinguish orogenic gold deposit scheelite from that from other types of mineral

521 deposits.

522   Strontium, Mo, Y and the REE, with the exception of Lu, are used in PCA and PLS-DA of orogenic gold deposit

523   scheelite against other types of deposits including gold, skarn, porphyry-related, greisen, breccia and polymetallic veins (Fig.

524   12 and ESM 3h). These elements were selected for the PCA and the PLS-DA, because they are more commonly reported.

525   The PCA yields PC1 with 56.0 %, PC2 with 19.4 % and PC3 with 11.4 % of the total variance (ESM 3h). PC1 is defined by

526   high positive contributions of the HREE including Gd, Tb, Dy, Ho, Er, Tm, Yb and Y, and high negative contributions of the

527   LREE including La, Ce, Pr and Nd. PC2 shows similar variation than PC1 and is defined by high negative contributions of

528   the HREE and Y and high positive contributions of the LREE. PC3 is defined by high positive contributions of Eu and Sr and

529   high negative contribution of Mo. Orogenic gold deposit scheelite has PC1 scores more similar to those from the other deposit

530   types (ESM 3h). Orogenic gold deposit scheelite commonly has positive PC3 scores, whereas scheelite from the other deposit

531   types commonly has negative PC3 scores. Thus, the PC1-PC3 space allows orogenic gold deposit scheelite to be distinguished

532   from scheelite from other deposit types (ESM 3ESM 3h). In the PC1-PC3 space, scheelite from Kochkar, Kumtor, Canadian

533   Malartic and Nevoria forms an intermediate group and overlaps with some greisen, skarn and polymetallic vein scheelite

534   (ESM 3h). Using PLS-DA (Fig. 12), $qw*_1$ is defined by positive contributions of Mo, La, Ce and Pr, and negative contributions

535   of Y, Sr and Eu, Gd, Tb, Dy, Ho, Er and Tm, whereas $qw*_2$ is defined by positive contributions of Mo and negative

536   contributions of Sr and Eu. Orogenic gold deposit scheelite has positive Eu and Sr, and negative Mo, contributions. Scheelite

537   from other types of deposits commonly has negative contributions of Eu and Sr, and positive contributions of Mo. The $qw*_1$-

538         $qw*_2$ loadings display distinct trace element compositions between orogenic gold deposit scheelite and that from the other

539   deposit types, which causes the sharp separation in t_1-t_2 space (Fig. 12). Strontium, Mo and Eu commonly have VIP greater

540   than 1 for each class (Fig. 12c), which shows that they are the main elements that contribute to deposit type discrimination.

541   On the other hand, REE and Y commonly have VIP lower than 0.8 (Fig. 12c), which shows that they do not contribute

542   significantly to deposit type discrimination. A combination of binary plots (Fig. 11), PCA (ESM 3ESM 3h), and PLS-DA

543   (Fig. 12), thus shows that the main elements that discriminate scheelite from orogenic gold deposits from that from other

544   deposit types are Sr, Mo, As and Eu. PCA and PLS-DA, combined with $(Gd/Yb)_{CN}$ vs $(La/Sm)_{CN}$ and $\sum$REE vs Eu*, show

545   that REE are not discriminant for orogenic gold deposit scheelite compared to that from the other deposit types. We conclude

546   that trace elements Sr, Mo, As, and Eu have high potential to discriminate orogenic gold deposit scheelite from that from

547   other deposit types. Thus, scheelite trace element composition has potential to orient exploration using indicator mineral

548   surveys. However, trace element data other than REE are not well characterized in scheelite from other deposit types, which

549   constrains the number of discriminant elements that can be studied here.

550   Nevoria has been ascribed to the orogenic gold deposit type by several authors (Eilu et al. 1999; Goldfarb et al. 2005)

551   but skarn by others (Mueller 1997; Mueller et al. 2004). Scheelite from the Nevoria gold deposit shows a different trace

552   element composition compared to scheelite from the other orogenic gold deposits including yellowish UVC colour, high Mo

553   concentration (Figs 8 and 11), low Sr/Mo ratio (Fig. 11), and a flat REE pattern without an Eu anomaly (Fig. 5). Scheelite

554   from Nevoria plot within the field associated with the other deposit types in PLS-DA (Fig. 12) and PCA (ESM 3h). This

555   shows that Nevoria's scheelite has a composition with a skarn affinity, consistent with the interpretation of Mueller 1997;

556   Mueller et al. 2004), providing a proof of concept for the scheelite chemical discrimination method.

557   **Conclusions**

558   Orogenic gold deposit scheelite is typically homogeneous in CL and exhibits a blue colour under short wave UVC

559   light, a characteristic of Mo-poor scheelite. Scheelite exhibits rare sector or oscillatory zoning and breccia texture that indicate

560   precipitation from hydrothermal fluids with different trace element compositions. Rare earth elements display five patterns

561   with a scheelite/chondrite average ratio near 100: a bell-shaped pattern with a i) positive or ii) negative Eu anomaly, iii) a flat

562   pattern with a positive Eu anomaly, and less commonly iv) a LREE-enriched pattern, and v) a HREE-enriched pattern. The

563   variation of REE patterns in scheelite suggests that scheelite-fluid REE fractionation is not the dominant processes controlling

564   scheelite composition, but, instead, that REE patterns are most probably controlled by the source of the hydrothermal fluid.

565   The bell-shaped and flat patterns are found in most of the orogenic gold deposits suggesting fluids with similar chemistry,

566   due to similar sources for the hydrothermal fluids. The Eu anomaly likely reflects the temperature of scheelite crystallization,

567   the substitution mechanism and the Na activity during crystallization. Scheelite from deposits hosted in low and moderate

568   metamorphic facies rocks commonly have high $\sum$REE+Y, Sr and Na, and low Mn and Nb+Ta+V contents, whereas scheelite

569   from deposits hosted in high metamorphic facies rocks commonly have low $\sum$REE+Y, Sr and Na, and high Mn and Nb+Ta+V

570   contents. The binary diagram $(Sr+Na)/(Sr+Na+10x(Nb+Ta+V+As))$ vs.

571     $((REE+Y)+10x(Nb+Ta+V+As))/(Sr+(REE+Y)+10x(Nb+Ta+V+As))$ enables scheelite from deposits hosted in low and

572   moderate metamorphic facies to be differentiated from scheelite from deposits hosted in high metamorphic facies rocks. As

573   well, PLS-DA allows scheelite from deposits hosted in low and moderate metamorphic facies rocks to be separated from

574   those from deposits hosted in high metamorphic facies rocks (Fig. 10e and f). Scheelite from deposits hosted in felsic to

575   intermediate rocks commonly have high $\sum$REE, Y and Na, and low Pb, Sr, U and Th concentrations, and a negative Eu

576   anomaly, whereas, scheelite from deposits hosted in sedimentary rocks have low $\sum$REE, Y and Na, and typically high Pb, Sr,

577   U and Th concentrations. PLS-DA separates scheelite from deposits hosted in felsic to intermediate rocks from that from

578   deposits hosted in sedimentary rocks. Both groups overlap partially with scheelite from deposits hosted in mafic-ultramafic

579   rocks. The overlap likely reflects the complex lithological packages hosting the deposits. Orogenic gold deposit scheelite REE

580 patterns cannot be distinguished from those of scheelite from other deposit types. Trace element composition, PCA, and PLS-

581 DA show a distinct trace element signatures in Sr, Mo, Eu, As and Sr/Mo for orogenic gold deposit scheelite, compared to

582 scheelite from other deposit types.

Acknowledgements

Figures captions

594 Fig. 1. Scheelite texture and mineral associations in orogenic gold deposits **a** aggregate of anhedral scheelite grains (Cuiaba,

595 Brazil), **b** subhedral scheelite grains (Canadian Malartic, Abitibi), **c** dynamic recrystallization of scheelite at Hutti (India), **d**

596 fine grains disseminated scheelite (Kochkar, Russia), **e** scheelite veins (Kumtor, Kyrgyzstan), **f** scheelite associated with

597 hydrothermal and metamorphic minerals such as clinopyroxene (Navachab, Namibia), **g** scheelite in association with

598 tourmaline (Essakane, Burkina Faso), **h** scheelite is associated with pyrite with gold inclusion at Tarmoola, Eastern Goldfields,

599 **i** scheelite with native gold, magnetite and hematite (Crusader, Australia).

600 Fig. 2. Cathodoluminescence (CL) images of scheelite show **a** homogeneous CL (Dome, Abitibi; the halo effect is an artefact

601 due to camera resolution), **b** sub-grains within larger scheelite (Essakane, Burkina Faso), **c** homogeneous fine grains (Hutti,

602 India), **d** homogenous scheelite cut by thin veinlets (Tarmoola, Yilgarn), **e** brecciated (Mount Pleasant, Southern Cross) **f**

603 brecciated structure at the edge of the grain (Crusader, Australia), **g** oscillatory zoning (Kochkar, Russia), **h** homogeneous CL

604 (Rosebel, Suriname), **i** oscillatory zoning (Crusader, Agnew district).

605   Fig. 3. Variation of the trace elements composition with the CL zonation in scheelite from the Macraes deposit, New Zealand.

606   **a** The CL shows two generations: the first generation labelled "1" is brecciated by the second generation labelled "2". **b** LA-

607   ICP-MS profile shows the trace element variation within the different scheelite generations. The first generation is

608   characterized by high Sr, Na, Mg, Mn, Th and U, and low Y and ∑REE content, whereas, the second generation is

609   characterized by low Sr, Na, Mg, Mn, Th and U, and high Y and ∑REE content. Zones 2a and 1b are too small to be quantified.

610   **c** The first generation is characterized by a flat REE pattern and the second generation is characterized by a bell-shaped REE

611   pattern, both with positive Eu anomalies.

612   Fig. 4. Images of scheelite **a** reflected light, **b** cathodoluminescence and trace elements LA-ICP-MS maps in **c** Sr, **d** Mo, **e**

613   Na, **f** Y, **g** Nb, **h** As, **i** Eu, **j** Gd and **k** Pb, show homogeneous composition typical for scheelite from orogenic gold deposits

614   (Dome, Abitibi).

615   Fig. 5. Rare earth element patterns in scheelite from orogenic gold deposits. **a** bell-shaped pattern with positive Eu anomaly,

616   **b** flat pattern with positive Eu anomaly, **c** bell-shaped with negative Eu anomaly, **d** LREE-enriched pattern, **e** HREE-enriched

617   pattern, **f** flat pattern without Eu anomaly. Data are normalized to chondrite from McDonough and Sun (1995). The North

618   American Shale Composite (NASC) values are from Gromet et al. (1984).

619   Fig. 6. Binary plots for REE contents in scheelite **a** (Gd/Yb)$_{CN}$ vs (La/Sm)$_{CN}$ and **b** ∑REE vs Eu* from orogenic gold deposits,

620   **c** (Gd/Yb)$_{CN}$ vs (La/Sm)$_{CN}$ and **d** ∑REE vs Eu* from various deposit types. Data for orogenic gold deposits from literature

621   include Ghaderi et al. (1999); Brugger et al. (2000b); Roberts et al. (2006); Xiong et al. (2006); Liu Yan et al. (2007); Dostal

622   et al. (2009); Song et al. (2014); Cave et al. (2016); Hazarika et al. (2016); Poulin (2016). Abbreviations: Bell + : bell-shaped

623   pattern with positive Eu anomaly; Bell -: bell-shaped pattern with negative Eu anomaly; Bell Ho + : bell-shaped pattern

624   centered in Ho with positive Eu anomaly as described in Dostal et al. (2009); Bell Ho - : bell-shaped pattern centered in Ho

625   with negative Eu anomaly as described in Dostal et al. (2009).

626   Fig. 7. LA-ICP-MS trace element binary plots for scheelite from orogenic gold deposits **a** ∑REE+Y vs Na; **b** Eu anomaly

627   (Eu*) vs Na; **c** Nb vs Ta; **d** ∑REE+Y vs Sr; **e** Na vs Sr, data for Rosebel are from EPMA; **f** Pb vs Sr; **g** ∑REE+Y vs Nb+Ta+V;

628   **h** ∑REE vs Y; **i** U vs Th. Data from the literature include Ghaderi et al. (1999) andDostal et al. (2009).

629   Fig. 8. Scheelite composition from orogenic gold and other deposit types for **a** Sr, **b** Mo, **c** Y and **d** Na. Literature data for

630   orogenic gold deposits are from Anglin et al. (1996); Ghaderi et al. (1999); Brugger et al. (2000b); Dostal et al. (2009);

631   Graupner et al. (2010); Hazarika et al. (2016); Poulin 2016; Poulin et al. (2016). Data for skarn deposits are from Eichhorn et

23

al. (1997); Zhigang et al. (1998); Liu Yan et al. (2007); Peng et al. (2010); Song et al. (2014); Poulin (2016); Poulin et al. (2016). Data for Greisen and VMS are from Poulin (2016). Abbreviation: Can. Malartic: Canadian Malartic.

Fig. 9. LA-ICP-MS trace element diagrams for scheelite in orogenic gold deposits **a** $(Sr+Na)/(Sr+Na+10x(Nb+Ta+V+As))$ vs $(REE+Y+10x(Nb+Ta+V+As))/(Sr+REE+Y+10x(Nb+Ta+V+As))$; **b** Fe-Mn-Mg scheelite composition measured by LA-ICP-MS; **c** Fe-Mn-Mg carbonate composition associated with scheelite in orogenic gold deposits, measured by EPMA.

Fig. 10. Partial Least Square-Discriminant Analysis of LA-ICP-MS data for scheelite in orogenic gold deposits. **a** qw^*_1-qw^*_2 and **b** t_1-t_2 scores for mineralization age; **c** qw_1^*-qw_2^* and **d** t_1-t_2 scores for host rock compositions; **e** qw^*_1-qw^*_2 and **f** t_1-t_2 scores for metamorphic facies of the host rocks. The qw^*_1-qw^*2 plots show the correlation between elements and the element contribution to each group. The t1-t2 plots show the distribution of scheelite sample according to each preselected grouping.

Fig. 11. LA-ICP-MS trace element binary plots for scheelite from orogenic gold deposits and other deposits types **a** Sr vs Eu anomaly (Eu*), **b** Sr/Mo vs Eu*, **c** Mo vs As, and **d** Sr/Mo vs As. Data for orogenic gold deposits: Ghaderi et al. (1999); Dostal et al. (2009); Cave et al. (2016); Hazarika et al. (2016); Poulin (2016). Data for skarn deposits: Xiong et al. (2006); Ren et al. (2010); Song et al. (2014); Guo et al. (2016); Poulin (2016); Fu et al. (2017), and for porphyry-related deposits: Poulin (2016) and Sun and Chen (2017).

Fig. 12. Partial Least Square-Discriminant Analysis of LA-ICP-MS data for scheelite from different deposit types. **a** The qw^*_1-qw^*_2 loadings plot shows correlations among elemental variables and deposit types. **b** The t_1-t_2 scores plot shows the distribution of scheelite samples in the qw^*_1-qw^*_2 space. **c** Variable importance of the projection (VIP) per deposit types shows the detailed element contribution per deposit. Data for orogenic gold deposits: Ghaderi et al. (1999); Dostal et al. (2009); Hazarika et al. (2016) and Poulin (2016), for skarn deposits: Song et al. (2014) and Poulin (2016) and for porphyry-related deposits: Poulin (2016) and Sun and Chen (2017).

Electronic Supplementary Materials captions

ESM 1. (a) Geological settings of the gold deposits; (b) Scheelite characteristics in the studied orogenic gold deposits

ESM 2. (a) Analytical conditions for trace element analyses in scheelite by EPMA; (b) EPMA elements composition in scheelite from orogenic gold deposits; (c) Analytical conditions for trace element analyses in scheelite by LA-ICP-MS; (d) LA-ICP-MS trace elements composition in scheelite from orogenic gold deposits

ESM 3. (a) Comparison between LA-ICP-MS and EPMA analyses for **a** Sr, **b** Mo, **c** Y and **d** Na. Red line − 1:1 ratio; abbreviation: DL: Detection limit of the electron microprobe; (b) Trace elements concentrations sorted by median scheelite composition for orogenic gold deposits, measured by LA-ICP-MS; (c) Carbonate coloration of samples with scheelite for deposits hosted in **a** low grade metamorphic facies rocks **b** moderate grade metamorphic facies rocks **c** high grade metamorphic facies rocks; (d) Variation of the trace elements composition with **a** the oscillatory zoning shown by CL in scheelite from the Crusader deposit, Agnew district (Australia). Zone 1 is characterized by **a** darker CL and high content in Na, V, As, Nb, Ta, Y and REE, and low Mo in **b**. Zone 2 is brighter CL and low content in Na, V, As, Nb, Ta, Y and REE, and higher Mo. **c** Both zones have a similar positive-slope REE pattern.; (e) Rare earth elements patterns from LA-ICP-MS data in scheelite from **a** Dome and Hollinger (Timmins, Canada); **b** Young Davidson (Matachewan, Canada); **c** Malartic (Canada), **d** Val-d'Or camp (Canada); **e** Meliadine (Canada); **f** Cuiaba (Brazil); **g** Buzwagi (Tanzania) and Essakane (Burkina Faso), **h** Hutti (India); **i** Kochkar (Russia); **j** Kumtor (Kyrgyzstan); (f) Rare earth elements patterns from LA-ICP-MS data in scheelite from **a** Marvel Loch (Australia); b Nevoria (Australia); **c** Edward's Find (Australia); **d** Crusader (Australia); **e** Tarmoola (Australia); **f** Paddington (Australia); **g** Mt Pleasant (Australia); **h** Norseman camp (Australia); **i** Mt. Charlotte (Australia); **j** Macraes (New Zealand); (g) Principal Component Analysis of LA-ICP-MS data for scheelite in orogenic gold deposits. Rare Earth Elements are reduced to ∑REE and Eu anomaly (Eu*). **a** PC1-PC2, **b** PC1-PC3 and **c** PC2-PC3 with emphasis on the mineralization age, **d** PC1-PC2, **e** PC1-PC3 and **f** PC2-PC3 with emphasis on the host rock composition, **g** PC1-PC2, **h** PC1-PC3 and **i** PC2-PC3 with emphasis on the metamorphic facies of the host rock; (h) Principal Component Analysis of LA-ICP-MS data for scheelite from different deposit types. Data from the literature for orogenic gold deposits: Dostal et al. (2009); Hazarika et al. (2016) and Poulin (2016), for skarn deposits: Song et al. (2014) and Poulin (2016), and for porphyry related deposits: Poulin (2016) and Sun and Chen (2017).

References

679   Alderton DHM, Pearce JA, Potts PJ (1980) Rare earth element mobility during granite alteration; evidence from Southwest

680   England. Earth Planet Sci Lett 49:149-165

681   Anglin CD (1992) Sm-Nd and Sr Isotopic Studies of Scheelite From Some Superior Province Gold Deposits Department of

682   Earth Sciences. Carleton University, Ottawa, pp 219

683   Anglin CD, Jonasson IR, Franklin J (1996) Sm-Nd dating of scheelite and tourmaline: Implications for the genesis of Archean

684   gold deposits, Val d'Or, Canada. Econ Geol 91:1372-1382

685   Aumo R, Salonen V-P (1986) Uvarovite and glacial transportation distance as provenance indicators of ore mineralization in

686   the southern part of the Outokumpu district, north Karelia, Finland Prospecting in Areas of Glaciated Terrain.

687   Institution of Mining and Metallurgy, London, pp 17-23

688   Beaudoin G, Pitre D (2005) Stable isotope geochemistry of the Archean Val-d'Or (Canada) orogenic gold vein field Miner

689   Deposita 40:59-75

690   Bell K, Anglin CD, Franklin JM (1989) Sm-Nd and Rb-Sr isotope systematics of scheelites: Possible implications for the age

691   and genesis of vein-hosted gold deposits. Geology 17:500-509

692   Boutroy E, Dare SAS, Beaudoin G, Barnes S-J, Lightfoot PC (2014) Magnetite composition in Ni-Cu-PGE deposits

693   worldwide: application to mineral exploration. J Geochem Explor 145:64-81

694   Brugger J, Giere R, Grobety B, Uspensky E (1998) Scheelite-powellite and paraniite-(Y) from the Fe-Mn deposit at Fianel,

695   Eastern Swiss Alps. Am Mineral 83:1100-1110

696   Brugger J, Bettiol AA, Costa S, Lahaye Y, Bateman R, Lambert DD, Jamieson DN (2000a) Mapping REE distribution in

697   scheelite using luminescence. Mineralogical Magazine 64:891-903

698   Brugger J, Lahaye Y, Costa S, Lambert D, Bateman R (2000b) Inhomogeneous distribution of REE in scheelite and dynamics

699   of Archaean hydrothermal systems (Mt. Charlotte and Drysdale gold deposits, Western Australia). Contrib Mineral

700   Petr 139:251-264

701   Brugger J, Maas R, Lahaye Y, McRae C, Ghaderi M, Costa S, Lambert D, Bateman R, Prince K (2002) Origins of Nd–Sr–Pb

702   isotopic variations in single scheelite grains from Archaean gold deposits, Western Australia. Chem Geol 182:203-

703   225

704   Brugger J, Etschmann B, Pownceby M, Liu WH, Grundler P, Brewe D (2008) Oxidation state of europium in scheelite:

705   Tracking fluid-rock interaction in gold deposits. Chem Geol 257:26-33

706   Burt DM (1989) Compositional and phase relations among rare earth elements. Reviews in Mineralogy 21:259-307

707   Cassidy KF, Bennett JM (1993) Gold mineralisation at the Lady Bountiful Mine, Western Australia; an example of a

708   granitoid-hosted Archaean lode gold deposit. Miner Deposita 28:388-408

709   Cave BJ, Pitcairn IK, Craw D, Large RR, Thompson JM, Johnson SC (2016) A metamorphic mineral source for tungsten in

710   the turbidite-hosted orogenic gold deposits of the Otago Schist, New Zealand. Miner Deposita Online

711   Condie KC (1993) Chemical composition and evolution of the upper continental crust: Contrasting results from surface

712   samples and shales. Chem Geol 104:1-37

713   Cottrant J (1981) Cristallochimie et geochimie des terres rares dans la scheelite: Application à quelques gisements français.

714   Université Pierre et Marie Curie,

715   Darbyshire DPF, Pitfield PEJ, Campbell SDG (1996) Late Archean and Early Proterozoic gold-tungsten mineralization in the

716   Zimbabwe Archean craton: Rb-Sr and Sm-Nd isotope constraints. Geology 24:19-22

717   Dare S, Barnes S-J, Beaudoin G, Méric J, Boutroy E, Potvin-Doucet C (2014) Trace elements in magnetite as petrogenetic

718   indicators. Miner Deposita 49:785-796

719   de Iorio M, Ebbels TMD, Stephens DA (2007) Statistical Techniques in Metabolic Profiling In: Balding DJ, Bishop MJ,

720   Cannings C (eds) Handbook of statistical genetics. 3rd ed edn. John Wiley & Sons, Chichester, England, pp 347-373

721   Dostal J, Kontak D, Chatterjee A (2009) Trace element geochemistry of scheelite and rutile from metaturbidite-hosted quartz

722   vein gold deposits, Meguma Terrane, Nova Scotia, Canada: genetic implications. Miner Petrol 97:95-109

723   Dupuis C, Beaudoin G (2011) Discriminant diagrams for iron oxide trace element fingerprinting of mineral deposit types.

724   Miner Deposita 46:319-335

725   Eichhorn R, Höll R, Jagout E, Schärer U (1997) Dating scheelite stages: A strontium, neodymium, lead approach from the

726   Felhertal tungsten deposit, Central Alps, Austria. Geochim Cosmochim Acta 61:5005-5022

727   Eilu PK, Mathison CI, Groves DI, Allardyce WJ (1999) Atlas of alteration assemblages, styles and zoning in orogenic lode-

728   gold deposits in a variety of host rock and metamorphic settings. University of Western Australia, Geology

729   Department and Extension Service, Perth, West. Aust., Australia

730   Fipke CE, Gurney JJ, Moore RO (1995) Diamond exploration techniques emphazising indicator mineral geochemistry and

731   Canadian examples. GSC Bull 423

732   Frei R, Nägler TF, Schönberg R, Kramers JD (1998) Re-Os, Sm-Nd, U-Pb, and stepwise lead leaching isotope systematics in

733   shear-zone hosted gold mineralization: genetic tracing and age constraints of crustal hydrothermal activity. Geochim

734   Cosmochim Acta 62:1925-1936

735   Fu Y, Sun X, Zhou H, Lin H, Jiang L, Yang T (2017) In-situ LA-ICP-MS trace elements analysis of scheelites from the giant

736   Beiya gold–polymetallic deposit in Yunnan Province, Southwest China and its metallogenic implications. Ore Geol

737   Rev 80:828-837

738 Garofalo PS, Fricker MB, Guenther D, Bersani D, Lottici PP (2014) Physical-chemical properties and metal budget of Au-

739 transporting hydrothermal fluids in orogenic deposits. Special Publication - Geological Society of London 402:71-

740 102

741 Ghaderi M, Palin JM, Campbell IH, Sylvester PJ (1999) Rare earth element systematics in scheelite from hydrothermal gold

742 deposits in the Kalgoorlie-Norseman region, Western Australia. Econ Geol 94:423-437

743 Goldfarb RJ, Baker T, Dube B, D. I. Groves, C. J. R. Hart, Gosselin P (2005) Distribution, character and genesis of gold

744 deposits in metamorphic terranes In: Hedenquist JW, Thompson JFH, Goldfarb RJ, Richards JP (eds) Economic

745 geology 100th Anniversary volume. pp 407–450

746 Goldfarb RJ, Groves DI (2015) Orogenic gold; common or evolving fluid and metal sources through time. Lithos (Oslo)

747 233:2-26

748 Graupner T, Niedermann S, Rhede D, Kempe U, Seltmann R, Williams C, Klemd R (2010) Multiple sources for mineralizing

749 fluids in the Charmitan gold(-tungsten) mineralization (Uzbekistan). Miner Deposita 45:667-682

750 Gromet LP, Dymek RF, Haskin LA, Korotev RL (1984) The "North American shale composite"; its compilation, major and

751 trace element characteristics. Geochim Cosmochim Acta 48:2469-2482

752 Guo Z, Li J, Xu X, Song Z, Dong X, Tian J, Yang Y, She H, Xiang A, Kang Y (2016) Sm/Nd dating and REE composition

753 of scheelite for the Honghuaerji scheelite deposit, Inner Mongolia, northeast China. Lithos (Oslo) 261:307-321

754 Gurney JJ (1984) A correlation between garnets and diamonds in kimberlites. University of Western Australia

755 Hancok MC, Robertson IG, Booth GW (1990) Paddington gold deposits In: Hughes FE (ed) Geology of Australian and Papua

756 New Guinean Mineral Deposits. Australasian Institute of Mining and Metallurgy Monograph 14,

757 Hazarika P, Mishra B, Pruseth KL (2016) Scheelite, apatite, calcite and tourmaline compositions from the late Archean Hutti

758 orogenic gold deposit: Implications for analogous two stage ore fluids. Ore Geol Rev 72:989-1003

759 Jochum KP, Nohl U, Herwig K, Lammel E, Stoll B, Hofmann AW (2005) GeoReM: A New Geochemical Database for

760 Reference Materials and Isotopic Standards. Geostand Geoanal Res 29:333-338

761 Johansson P, Keinänen V, Lehmuspelto P (1986) Geochemical exploration of tungsten in glaciogenic deposits in Soretiapulju,

762 western Finnish Lapland Prospecting in Areas of Glaciated Terrain. Institution of Mining and Metallurgy, London,

763 pp 61-67

764 Jowitt SM, Cooper K, Squire RJ, Thébaud N, Fisher L, Cas RAF, Pegg I (2014) Geology, mineralogy, and geochemistry of

765 magnetite-associated Au mineralization of the ultramafic–basalt greenstone hosted Crusader Complex, Agnew Gold

766 Camp, Eastern Yilgarn Craton, Western Australia; a Late Archean intrusion-related Au deposit ? Ore Geol Rev

767 56:53-72

768 Kempe U, Belyatsky B, Krymsky R, Kremenetsky AA, Ivanov PA (2001) Sm-Nd and Sr isotope systematics of scheelite

769   from the giant Au(-W) deposit Muruntau (Uzbekistan): implications for the age and sources of Au mineralization.

770   Miner Deposita 36:379-392

771 Kent AJR, Campbell IH, McCulloch MT (1995) Sm-Nd systematics of hydrothermal scheelite from the Mount Charlotte

772   Mine, Kalgoorlie, Western Australia; an isotopic link between gold mineralization and komatiites. Econ Geol

773   90:2329-2335

774 Kerrich R, Fryer BJ (1978) Archaean precious-metal hydrothermal systems, Dome Mine, Abitibi greenstone belt; II, REE and

775   oxygen isotope relations. Can J Earth Sci 16:440-458

776 Kolb J, Sindern S, Kisters AFM, Michael Meyer F, Hoernes S, Schneider J (2005) Timing of Uralian orogenic gold

777   mineralization at Kochkar in the evolution of the East Uralian granite-gneiss terrane. Miner Deposita 40:473-491

778 Lindmark B (1977) Till-sampling methods used in exploration for scheelite in Kaustinen, Finland Prospecting in Areas of

779   Glaciated Terrain. Institute of Mining and Metallurgy, Helsinki

780 Liu W, Etschmann B, Migdisov A, Boukhalfa H, Testemale D, Mueller H, Hazemann J-L, Brugger J (2017) Revisiting the

781   hydrothermal geochemistry of europium(II/III) in light of new in situ XAS spectroscopy results. Chem Geol 459:61-

782   74

783 Liu Yan, Deng Jun, Li ChaoFeng, Shi GuangHai, AiLi Z (2007) REE composition in scheelite and scheelite Sm-Nd dating

784   for the Xuebaoding W-Sn-Be deposit in Sichuan. Chin Sci Bull 52:2543-2550

785 MacRae CM, Wilson NC, Brugger J (2009) Quantitative Cathodoluminescence Mapping with Application to a Kalgoorlie

786   Scheelite. Microscopy and Microanalysis 15:222-230

787 Mao J, Konopelko D, Seltmann R, Lehmann B, Chen W, Wang Y, Eklund O, Usubaliev T (2004) Postcollisional age of the

788   Kumtor gold deposit and timing of Hercynian events in the Tien Shan, Kyrgyzstan. Econ Geol 99:1771-1780

789 McClenaghan MB, Kjarsgaard BA (2007) Indicator mineral and surficial geochemical exploration methods for kimberlite in

790   glaciated terrain; Examples from Canada In: Goodfellow WD (ed) Mineral Deposits of Canada: A Synthesis of Major

791   Deposit-Types, District Metallogeny, the Evolution of Geological Provinces, and Exploration Methods. Geological

792   Association of Canada, Mineral Deposits Division,

793 McClenaghan MB, Cabri LJ (2011) Review of gold and platinum group element (PGE) indicator minerals methods for

794   surficial sediment sampling. Geochem: Explor, Environ, Anal 11:251-263

795 McDonough WF, Sun Ss (1995) The composition of the Earth. Chem Geol 120:223-253

796 Mortensen JK, Craw D, MacKenzie DJ, Gabites JE, Ullrich T (2010) Age and origin of orogenic gold mineralization in the

797   Otago schist belt, South Island, New Zealand; constraints from lead isotope and (super 40) Ar/ (super 39) Ar dating

798   studies. Econ Geol 105:777-793

799 Mueller AG (1991) The Savage Lode magnesian skarn in the Marvel Loch gold-silver mine, Southern Cross greenstone belt,

800   Western Australia; Part 1, Structural setting, petrography, and geochemistry. Can J Earth Sci 28:659-685

801 Mueller AG, De Laeter JR, Groves DI (1991a) Strontium isotope systematics of hydrothermal minerals from epigenetic

802   Archean gold deposits in the Yilgarn Block, Western Australia. Econ Geol 86:780-809

803 Mueller AG, Groves DI, Delor CP (1991b) The Savage Lode magnesian skarn in the Marvel Loch gold-silver mine, Southern

804   Cross greenstone belt, Western Australia; Part 2, Pressure-temperature estimates and constraints on fluid sources.

805   Can J Earth Sci 28:686-705

806 Mueller AG (1992) Petrogenesis of amphibole-biotite-calcite-plagioclase alteration and laminated gold-silver quartz veins in

807   four Archean shear zones of the Norseman District, Western Australia. Canadian Journal of Earth Sciences = Revue

808   Canadienne des Sciences de la Terre 29:388-417

809 Mueller AG (1997) The Nevoria gold skarn deposit in Archean iron-formation, Southern Cross greenstone belt, Western

810   Australia; I, Tectonic setting, petrography, and classification. Econ Geol 92:181-209

811 Mueller AG, Nemchin AA, Frei R (2004) The Nevoria gold skarn deposit, Southern Cross greenstone belt, Western Australia;

812   II, Pressure-temperature-time path and relationship to postorogenic granites. Econ Geol 99:453-478

813 Mueller AG (2015) Structure, alteration, and geochemistry of the Charlotte quartz vein stockwork, Mt Charlotte gold mine,

814   Kalgoorlie, Australia; time constraints, down-plunge zonation, and fluid source. Miner Deposita 50:221-244

815 Nassau K (1963) Calcium tungstate—IV: The theory of coupled substitution. J Phys Chem Solids 24:1511-1517

816 Nassau K, Loiacono GM (1963) Calcium tungstate—III: Trivalent rare earth substitution. J Phys Chem Solids 24:1503-1510

817 Peltonen P, Huhta P, Korsman K (1992) Occurrence and mineral chemistry of chrome spinel in till - implications for

818   prospecting magmatic Ni-Cu sulfide ores in Svecofennian terrain. Geological Survey of Finland,

819 Peng J, Zhang D, Hu R, Wu M, Lin Y (2010) Sm/Nd and Sr isotope geochemistry of hydrothermal scheelite from the Zhazixi

820   W-Sb deposit, western Hunan. Acta Geol Sinica 82:1514-1521

821 Poulin R, S. (2016) A study of the crystal chemistry, cathodoluminescence, geochemistry and oxygen isotopes in scheelite:

822   Application towards discriminating among differing ore-deposit systems Geology. Laurentian University, Sudbury,

823   Ontario, Canada

824   Poulin R, S., McDonald AM, Kontak DJ, McClenaghan MB (2016) On the Relationship Between Cathodoluminescence and

825   the Chemical Composition of Scheelite From Geologically Diverse Ore-Deposit Environments. Can Mineral

826   54:1147-1173

827   Poulin RS, Kontak DJ, McDonald A, McClenaghan MB (2018) Assessing scheelite as an ore-deposit discriminator using its

828   trace-element and REE chemistry. The Canadian Mineralogist 56:265-302

829   Raimbault L, Baumer A, Dubru M, Benkerrou C, Croze V, Zahm A (1993) REE fractionation between scheelite and apatite

830   in hydrothermal conditions. Am Mineral 78:1275-1285

831   Ren YS, Zhao HL, Lei E, Wang H, Ju N, Wu CZ (2010) Trace element and rare earth element geochemistry of the scheelite

832   and ore genesis of the Yangjingou large scheelite deposit in Yanbian area, northeastern China. China Acta Petrol Sin

833   26:3720–3726

834   Ridley JR, Diamond LW (2000) Fluid Chemistry of Orogenic Lode Gold Deposits and Implications for Genetic Models In:

835   Hagemann SG, Brown PE (eds) Gold in 2000 - Reviews in Economic Geology 13. Society of Economic Geologists,

836   Roberts S, Palmer MR, Waller L (2006) Sm-Nd and REE characteristics of tourmaline and scheelite from the Bjorkdal gold

837   deposit, northern Sweden: Evidence of an intrusion-related gold deposit? Econ Geol 101:1415-1425

838   Scanlan EJ, Scott JM, Wilson VJ, Stirling CH, Reid MR, Le Roux PJ (2018) In situ (super 87) Sr/ (super 86) Sr of scheelite

839   and calcite reveals proximal and distal fluid-rock interaction during orogenic W-Au mineralization, Otago Schist,

840   New Zealand. Econ Geol 113:1571-1586

841   Schwebel PJ, King P, Eisenlohr BN (1995) Edwards Find gold deposit Southern Cross greenstone belt - Geology and gold

842   mines. Southern Cross, Western Australia, pp 75-80

843   Shi W, Fleet ME, Sheih SR (2012) High-pressure phase transitions in Ca-Mn carbonates $(Ca,Mn)CO_3$ studied by Raman

844   spectroscopy. Am Mineral 97:999-1001

845   Shoji T, Sasaki N (1978) Fluorescent color and X-ray powder data of synthesized scheelite-powellite series as guides to

846   determine its composition. Kozan Chishitsu = Mining Geology 28, (6):397-404

847   Somarin AK (2004) Garnet composition as an indicator of Cu mineralization: evidence from skarn deposits of NW Iran. J

848   Geochem Explor 81:47-57

849   Song G, Qin K, Li G, Evans NJ, Chen L (2014) Scheelite elemental and isotopic signatures; implications for the genesis of

850   skarn-type W-Mo deposits in the Chizhou area, Anhui Province, eastern China. Am Mineral 99:303-317

851   Sun K, Chen B (2017) Trace elements and Sr-Nd isotopes of scheelite; implications for the W-Cu-Mo polymetallic

852   mineralization of the Shimensi Deposit, south China. Am Mineral 102:1114-1128

853   Sverjensky DM (1984) Europium redox equilibrium in aqueous solutions. Earth Planet Sci Lett 67:70-78

854   Sylvester PJ, Ghaderi M (1997) Trace element analysis of scheelite by excimer laser ablation-inductively coupled plasma-

855   mass spectrometry (ELA-ICP-MS) using a synthetic silicate glass standard. Chem Geol 141:49-65

856   Toverud Ö (1984) Dispersal of tungsten in glacial drift and humus in Bergslagen, southern central Sweden. J Geochem Explor

857   21:261-272

858   Tyson RM, Hemphill WR, Theisen AF (1988) Effect of the W:Mo ratio on the shift of excitation and emission spectra in the

859   scheelite-powellite series. Am Mineral 73:1145-1154

860   Uspensky E, Brugger J, Graeser S (1998) REE geochemistry systematics of scheelite from the Alps using luminescence

861   spectroscopy: from global regularities to local control. Schweizerische Mineralogische Und Petrographische

862   Mitteilungen 78:31-54

863   Van Horn FR (1930) Replacement of wolframite by scheelite with observations on the fluorescence of certain tungsten

864   minerals. Am Mineral 15:461-469

865   Voicu G, Bardoux M, Stevenson R, Jebrak M (2000) Nd and Sr isotope study of hydrothermal scheelite and host rocks at

866   Omai, Guiana Shield: implications for ore fluid source and flow path during the formation of orogenic gold deposits.

867   Miner Deposita

868   Xiong DX, Sun XM, Shi GY, Wang SW, Gao JF, Xue T (2006) Trace elements, rare earth elements (REE) and Nd-Sr isotopic

869   compositions in scheelites and their implications for the mineralization in Daping gold mine in Yunnan province,

870   China. China Acta Petrol Sin 22:733-741

871   Zhigang Z, Chaoyang L, Yuping L, Guangzhi T (1998) REE geochemistry of scheelite of two genetic types from Nanyangtian,

872   southeastern Yunnan, China. Geology-Geochemistry 26:34-38

873

Figure 1

Figure 2

Figure 3
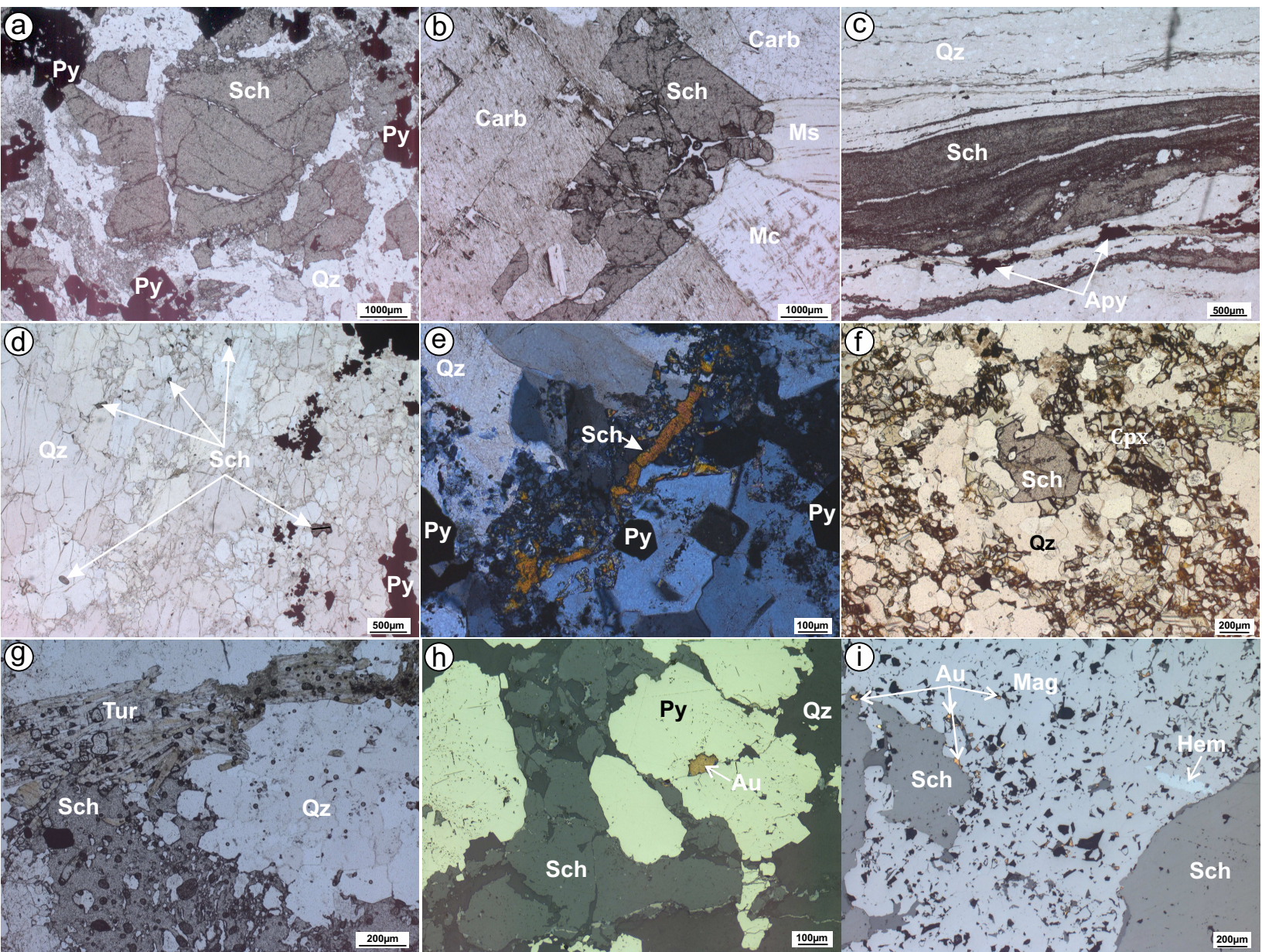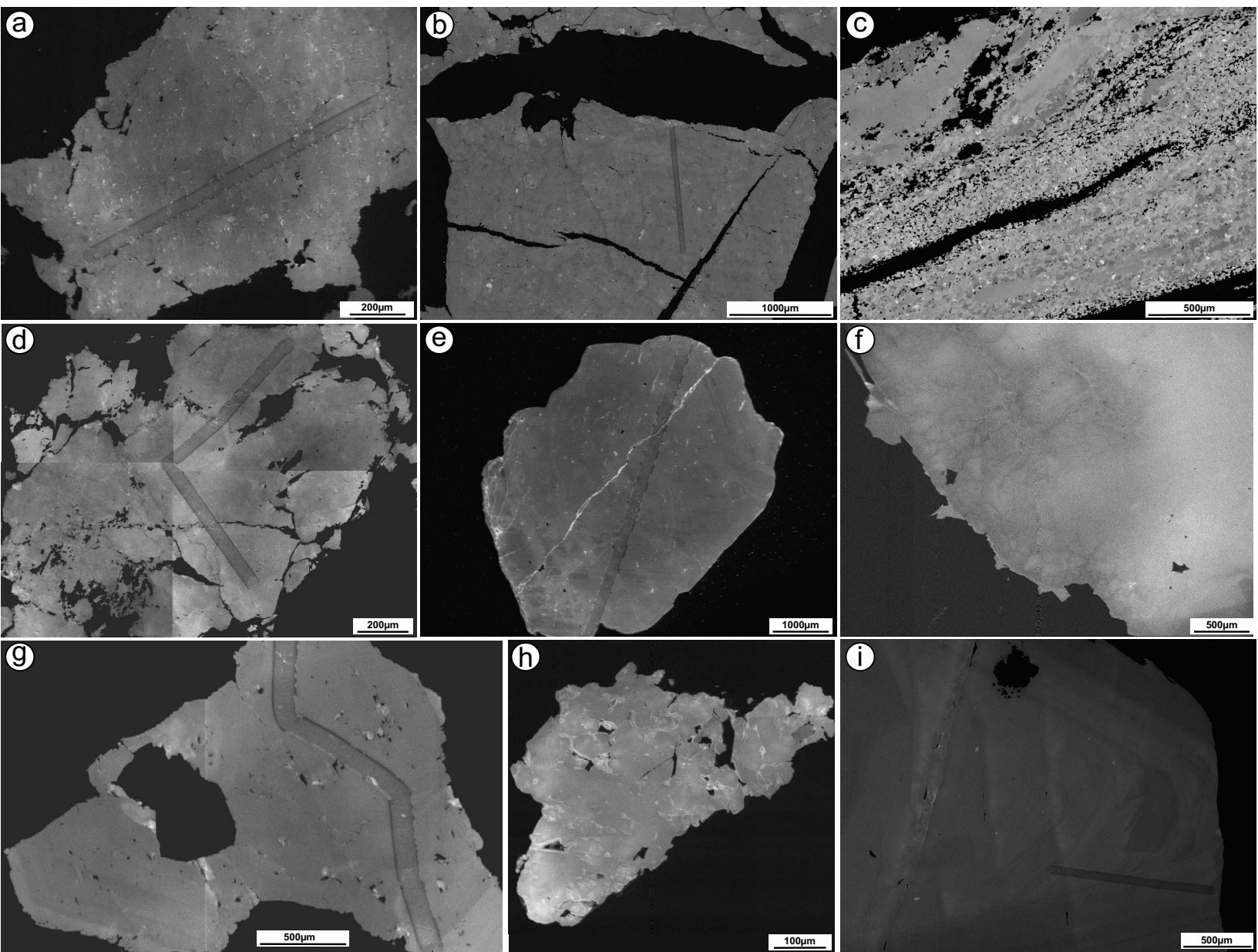
MACR01D-L3			
ppm	1a	2b	1c
Sr	5130	2250	7050
Na	68.0	40.0	62.5
Mg	21.8	11.4	17.5
Mn	4.31	1.22	6.01
Th	0.523	0.056	0.432
U	1.360	0.053	0.766
Y	115	536	166
∑REE	137.44	643.10	181.93
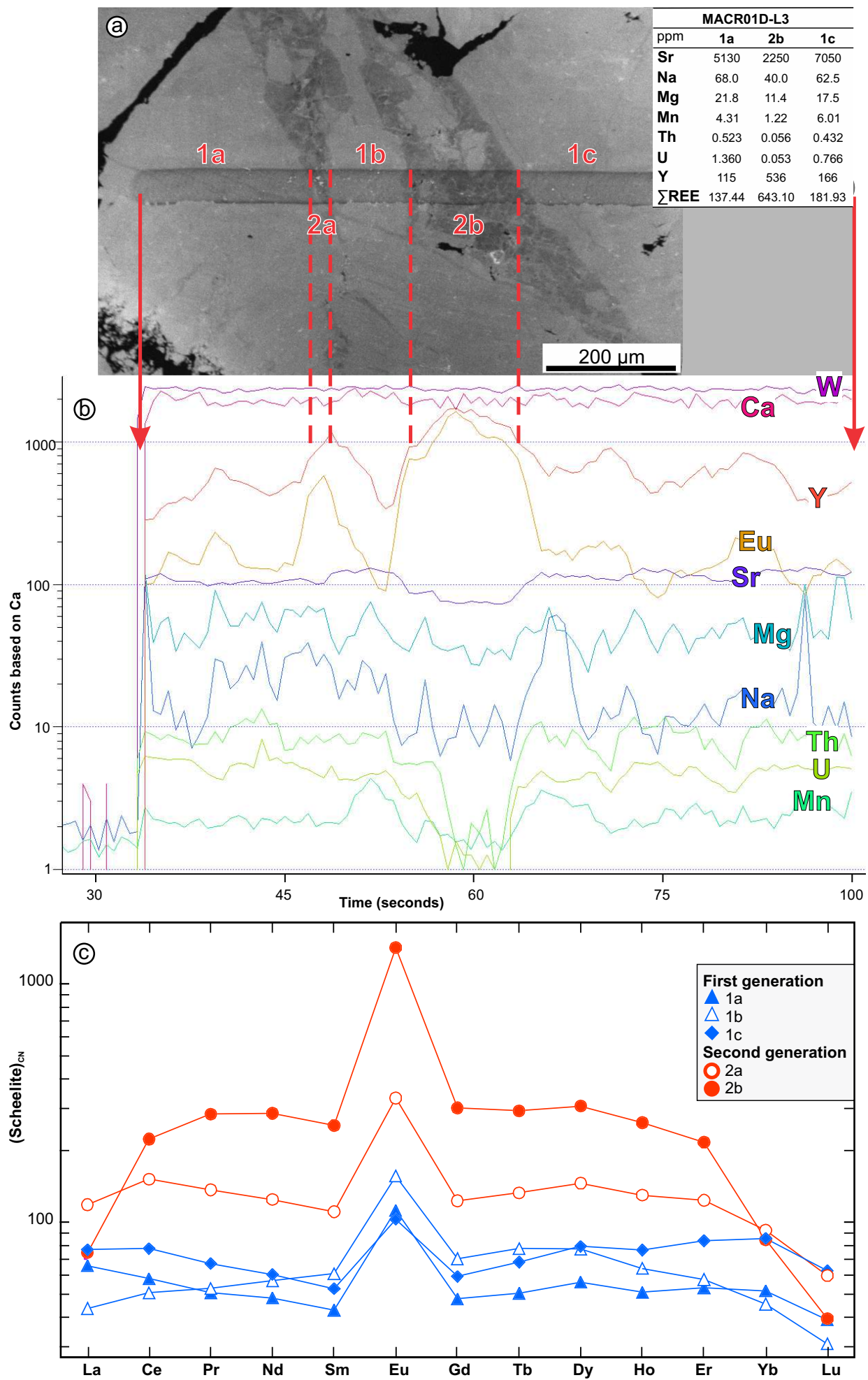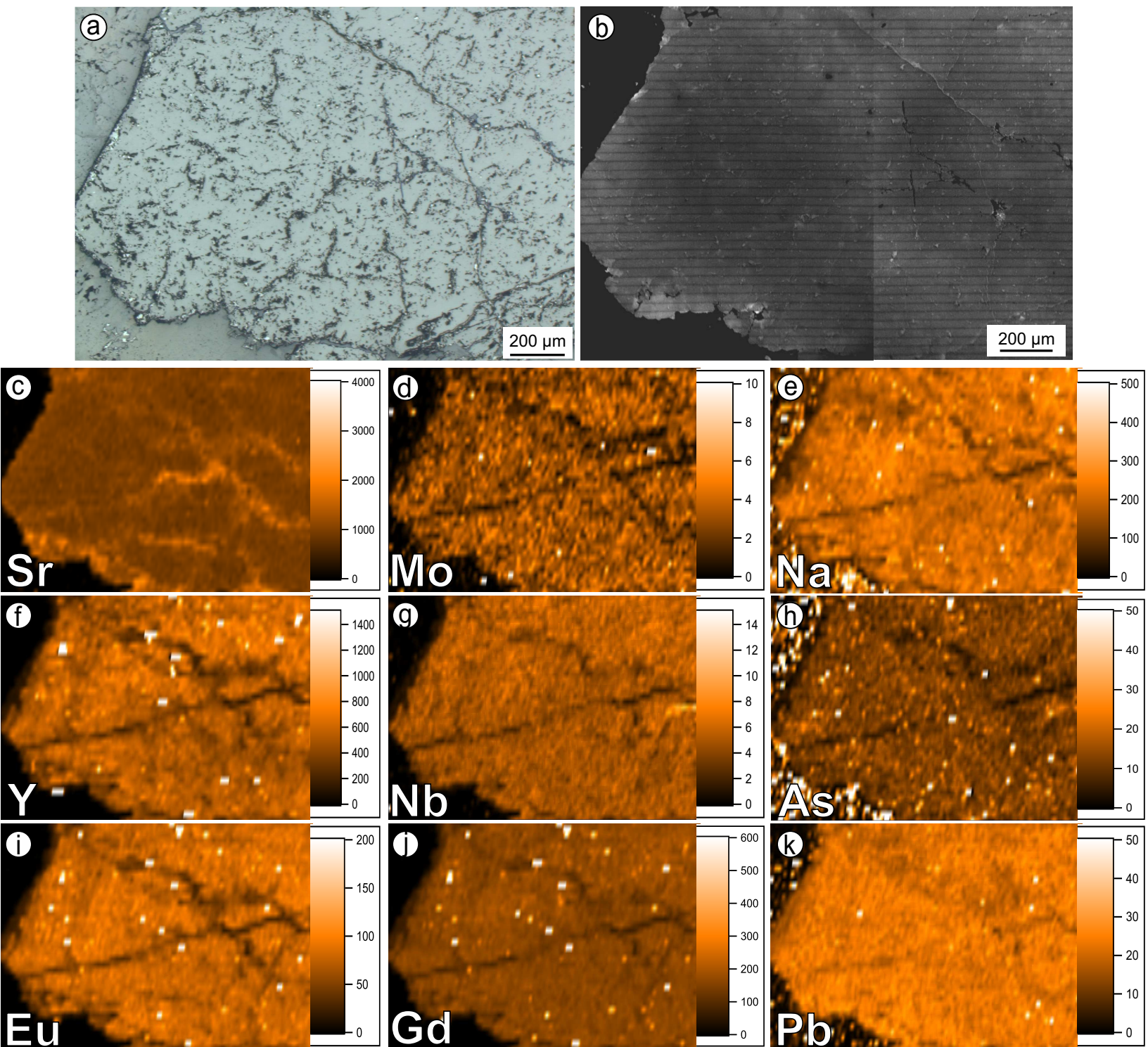
Figure 3

Figure 4

Figure 5

Figure 5
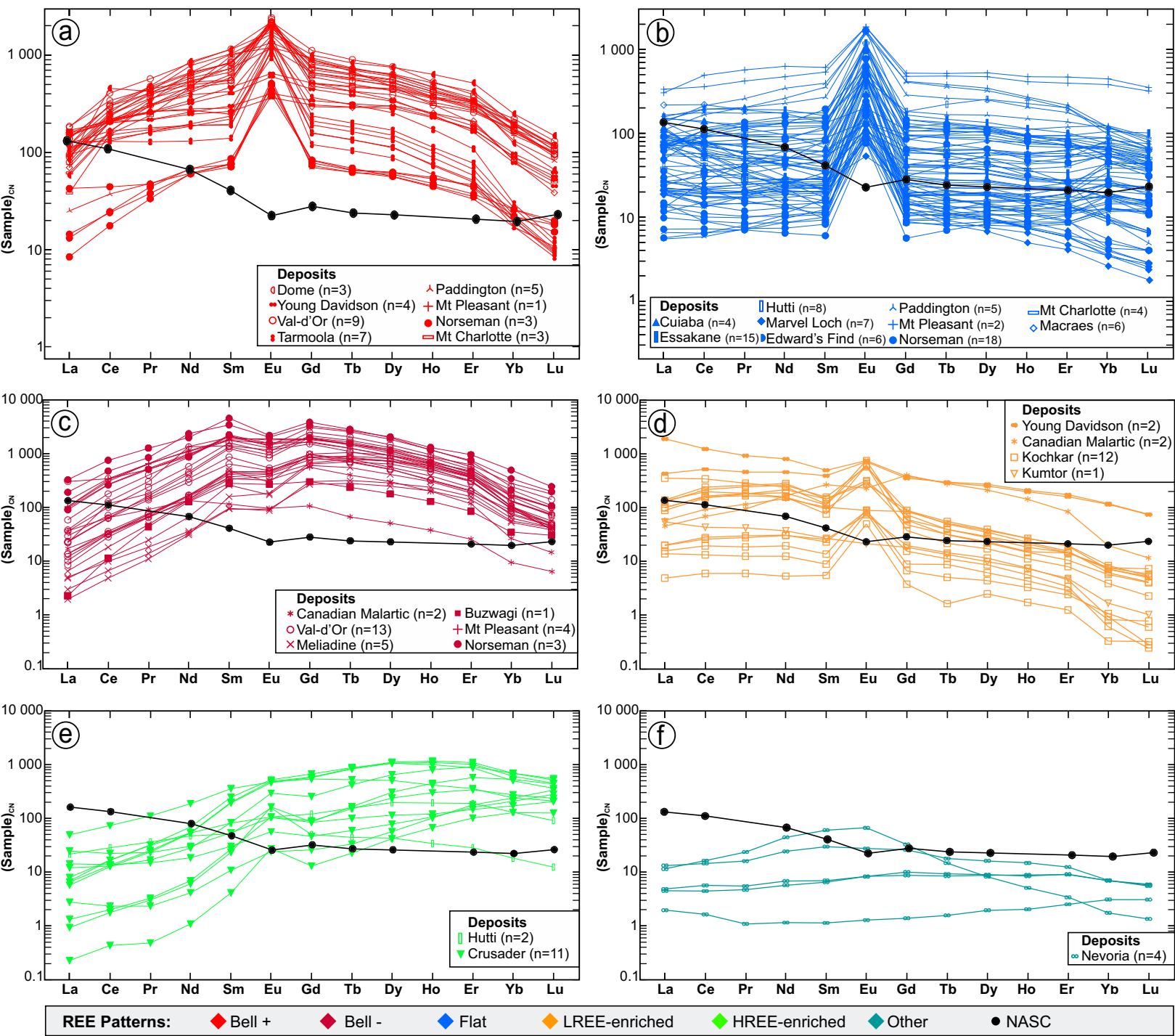
Figure 6
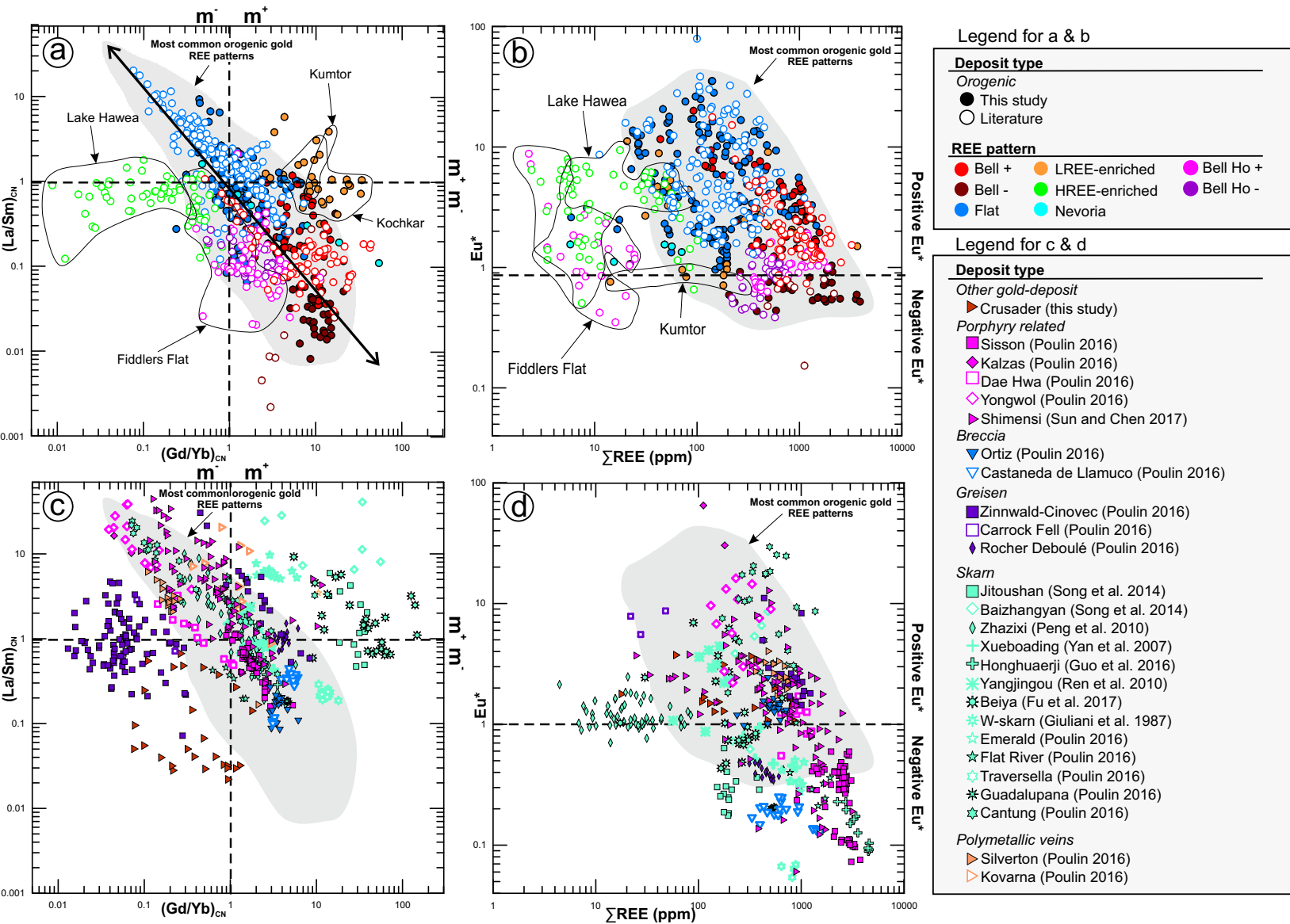
Figure 7

Figure 7
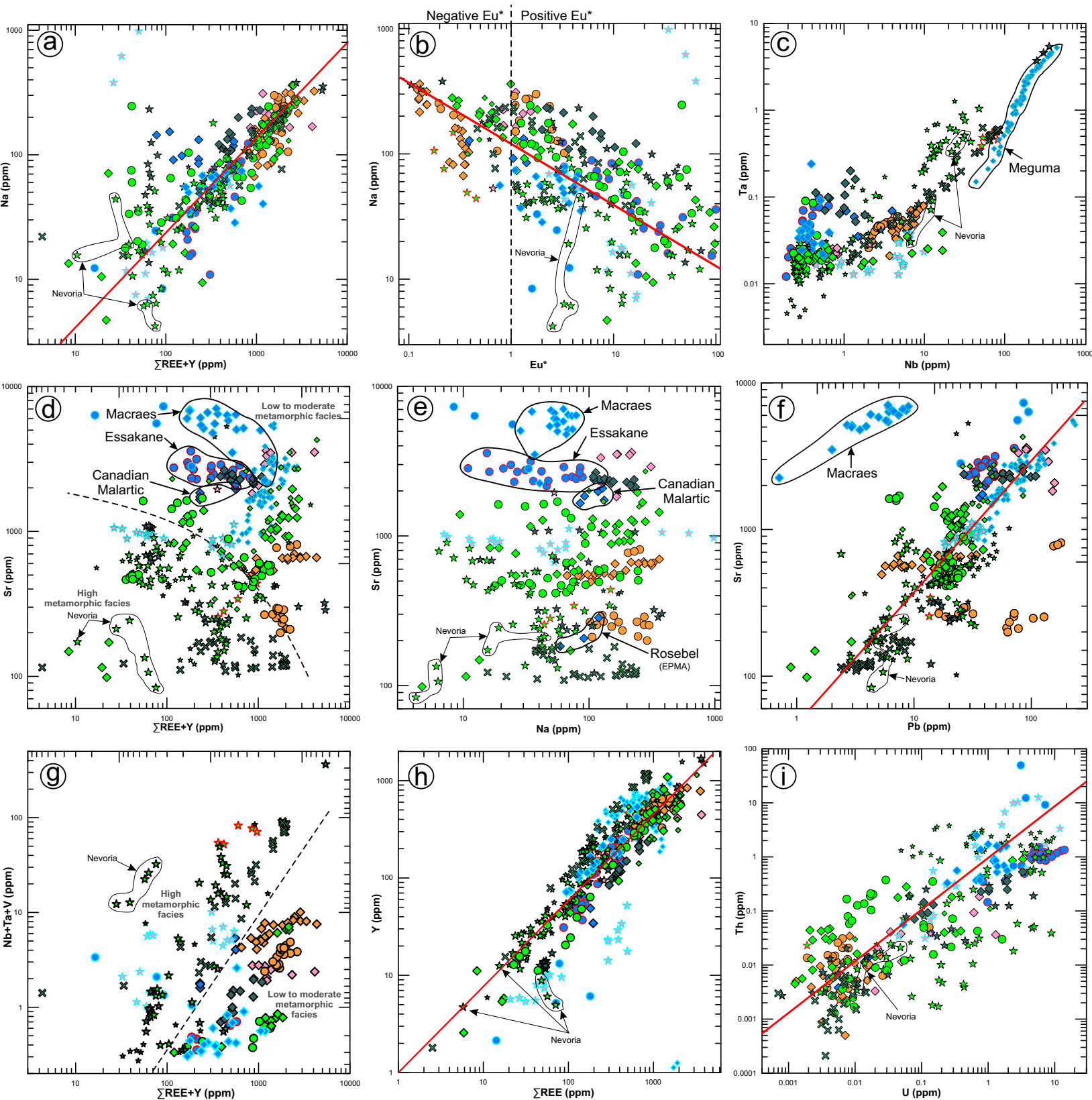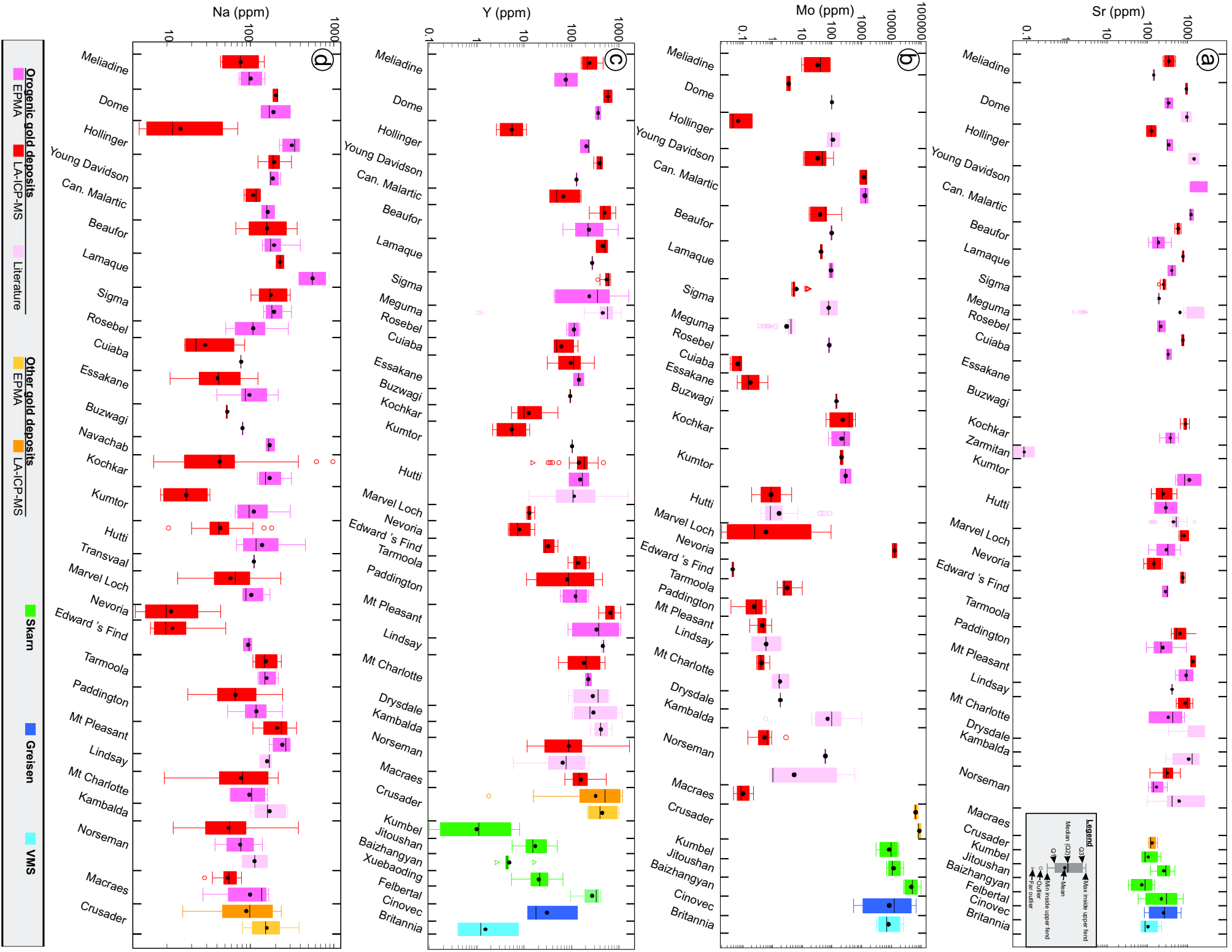
Figure 7

Figure 8

Figure 9

Figure 9
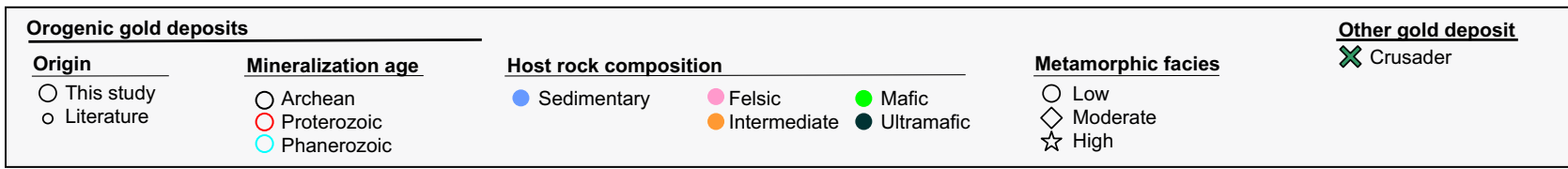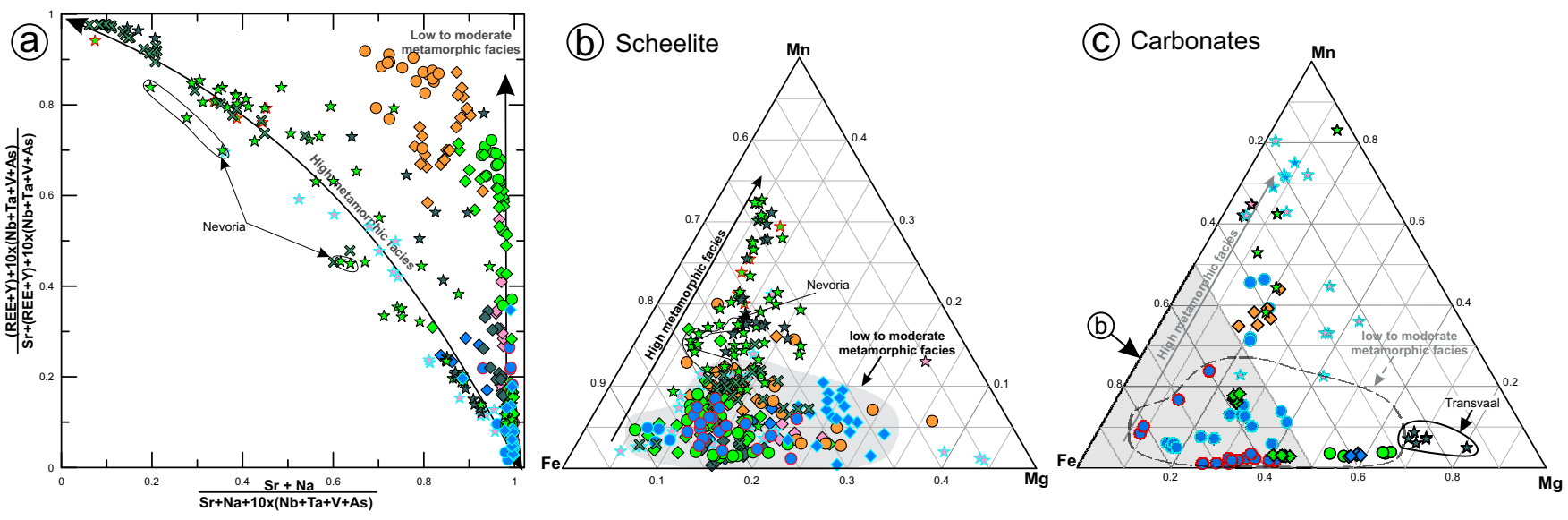
Figure 10
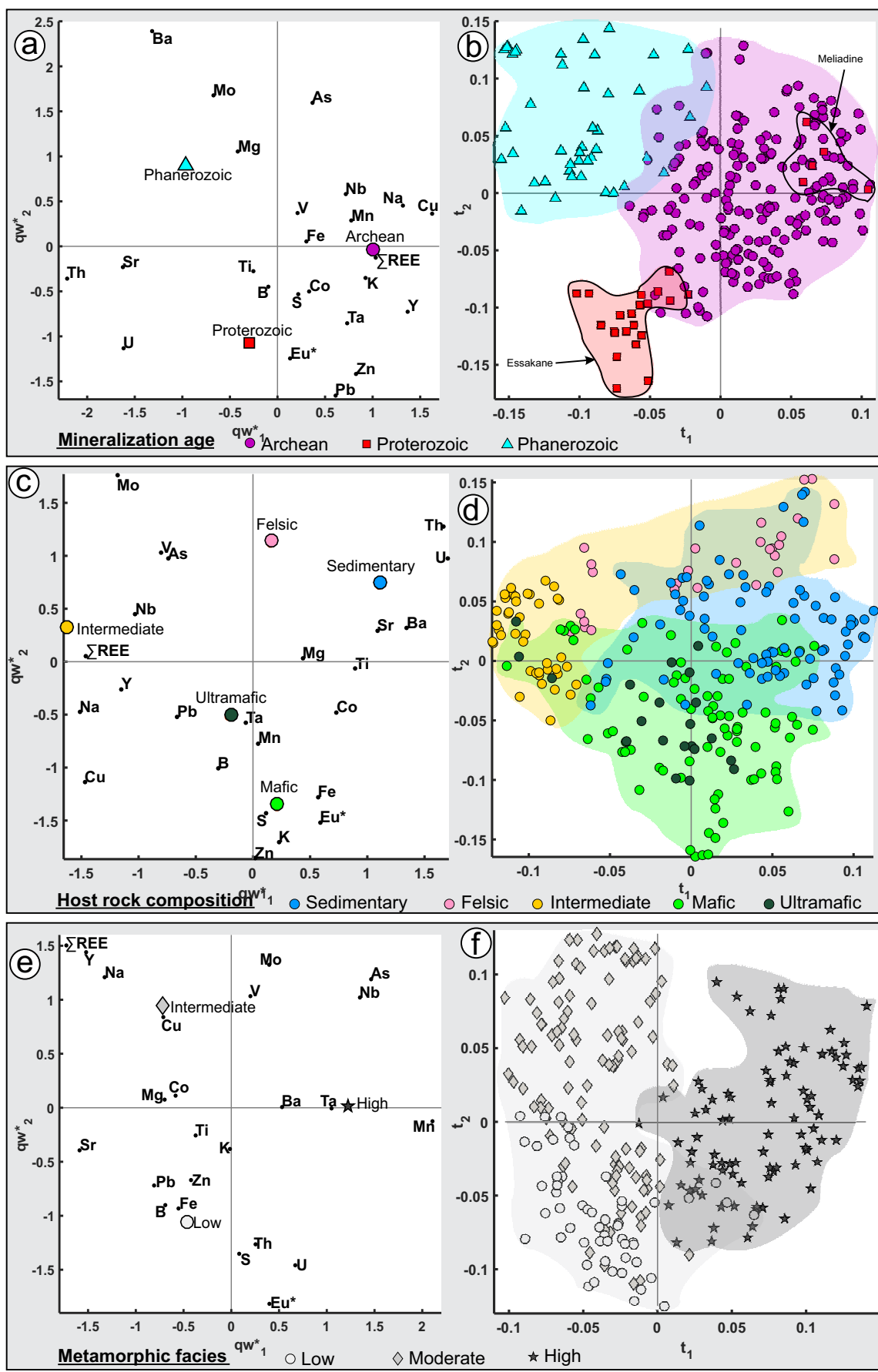
Figure 10

Figure 11

Figure 11
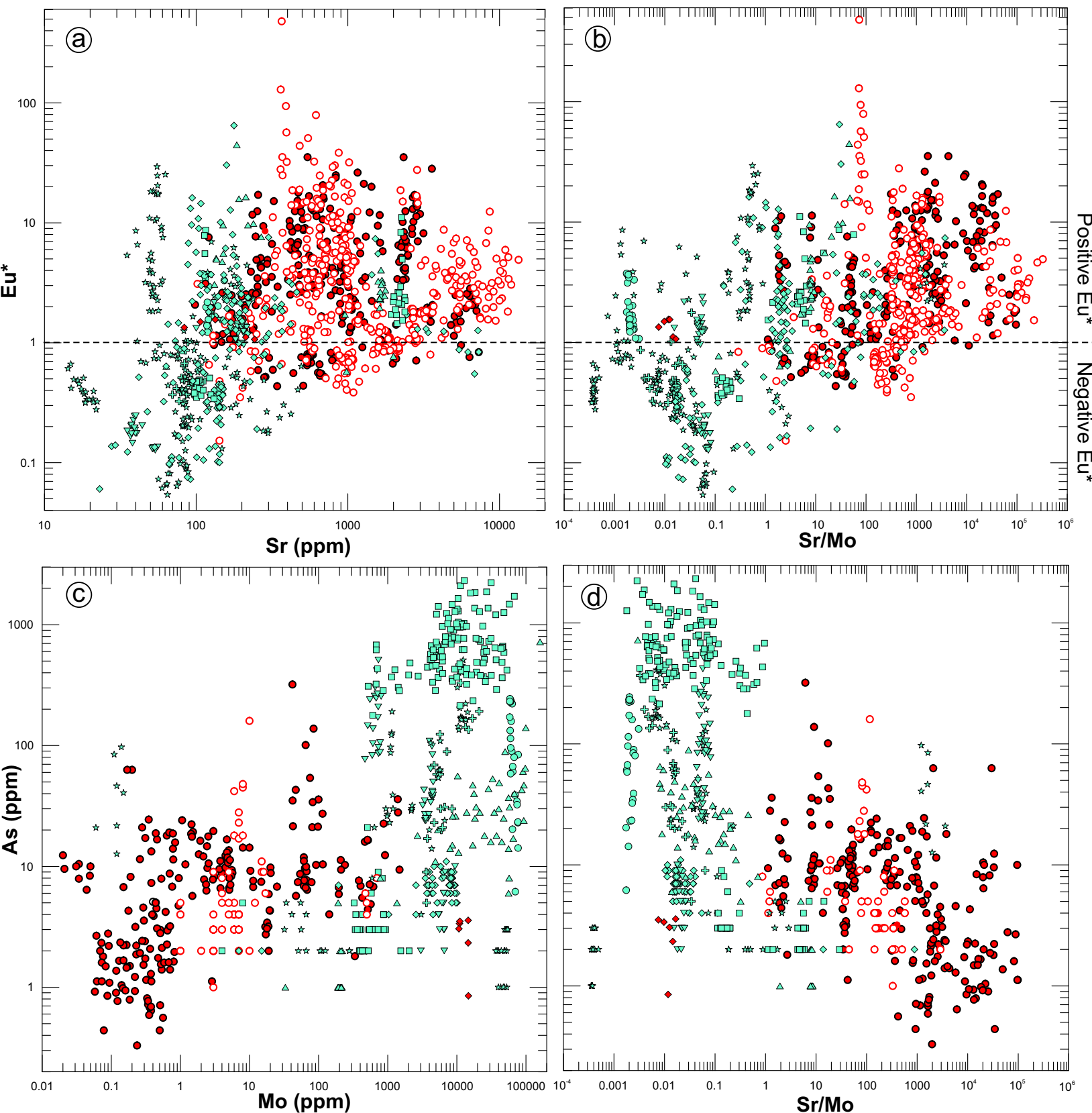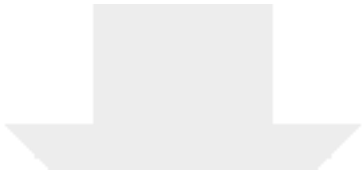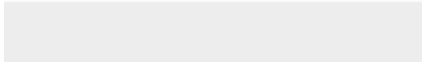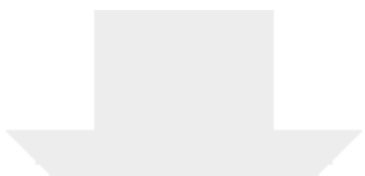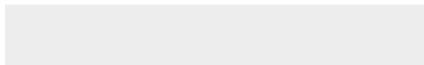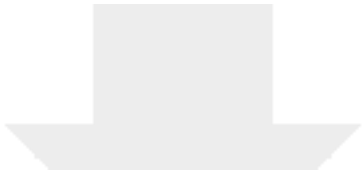

Figure 11

Figure 12

Figure 12
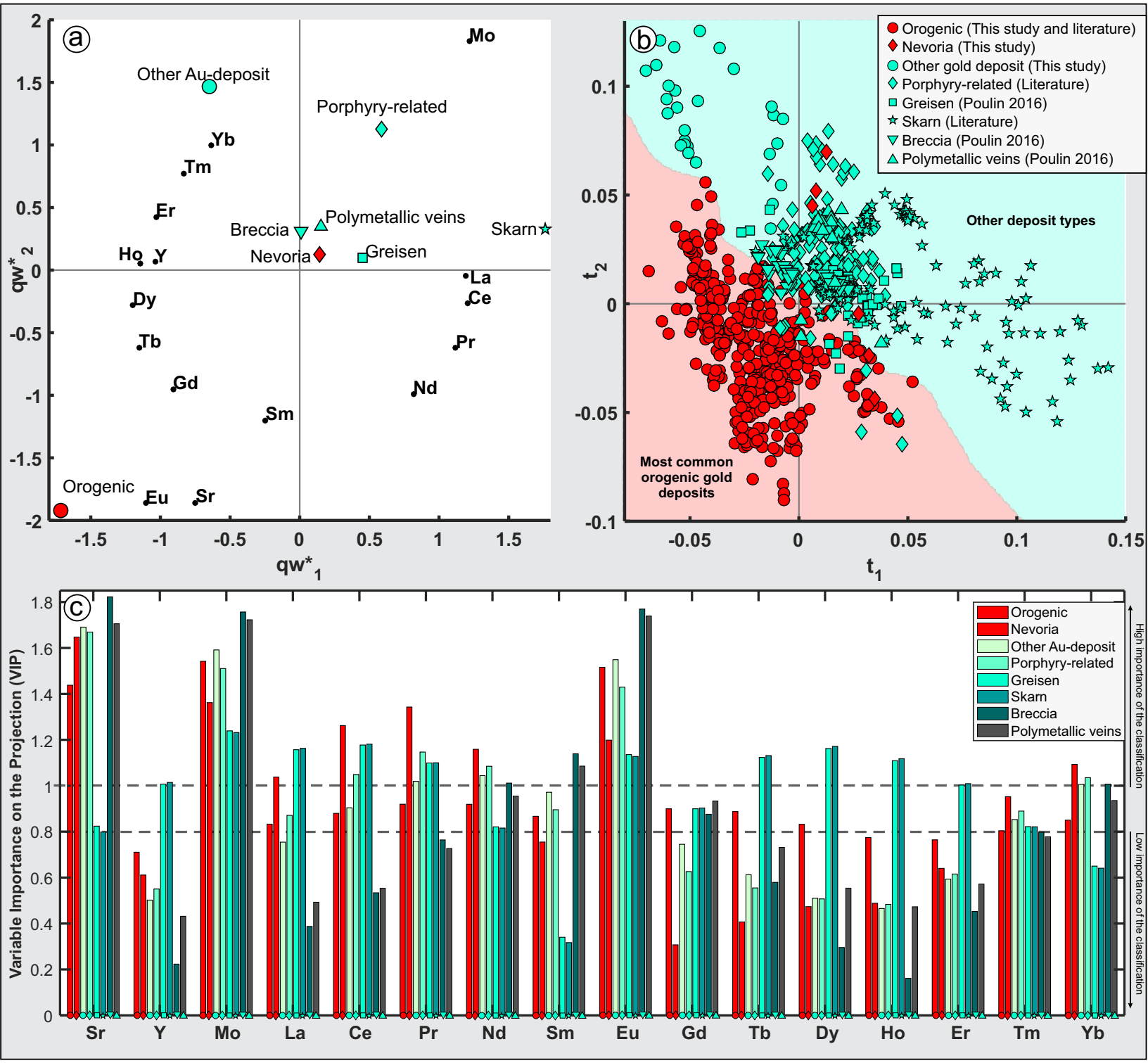
Click here to access/download
Supplementary Material
ESM01.pdf

Click here to access/download
Supplementary Material
ESM02.xlsx

Click here to access/download
Supplementary Material
ESM03.pdf